



The Abdus Salam
International Centre
for Theoretical Physics

ICTP Diploma Programme

Earth System Physics

Seismology

Seismic sources – 3

Focal mechanisms

Fabio ROMANELLI

Dept. Mathematics & Geosciences

Università degli studi di Trieste

romanel@units.it



Seismic sources - 3



Focal mechanisms

- faulting and radiation pattern
- fault mechanism
- decomposition of moment tensor
- basic fault plane solutions
- faults and plates

Haskell model

- far field for an extended source
- directivity
- source spectra



Final source representation



$$u_n(\mathbf{x}, t) = \iint_{\Sigma} [u_i] c_{ijpq} v_j * \frac{\partial G_{np}}{\partial \xi_q} d\Sigma$$

$$m_{pq} = [u_i] c_{ijpq} v_j \quad u_n(\mathbf{x}, t) = \iint_{\Sigma} m_{pq} * \frac{\partial G_{np}}{\partial \xi_q} d\Sigma$$

And if the source can be considered a point-source (for distances greater than fault dimensions), the contributions from different surface elements can be considered in phase. Thus for an effective **point source**, one can define the **moment tensor**:

$$M_{pq} = \iint_{\Sigma} m_{pq} d\Sigma$$
$$u_n(\mathbf{x}, t) = M_{pq} * G_{np,q}$$



A particular case - moment tensor



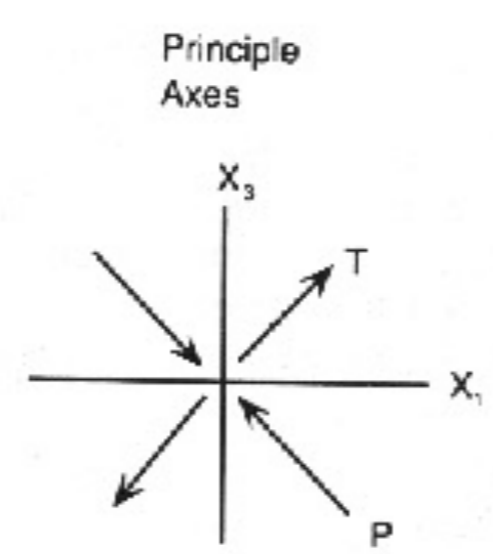
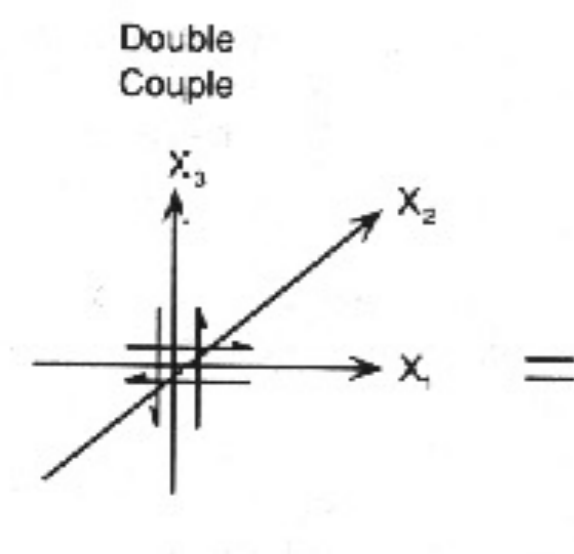
$$\mathbf{m} = \begin{pmatrix} 0 & 0 & \mu[u_1(\xi, \tau)] \\ 0 & 0 & 0 \\ \mu[u_1(\xi, \tau)] & 0 & 0 \end{pmatrix}$$

$$\mathbf{M} = \begin{pmatrix} 0 & 0 & M_0 \\ 0 & 0 & 0 \\ M_0 & 0 & 0 \end{pmatrix}$$

$$\phi=0^\circ, \delta=0^\circ, \lambda=0^\circ$$

$$\mathbf{u} = \begin{cases} [\bar{u}] \hat{\mathbf{e}}_x \\ 0 \\ 0 \end{cases} \quad \mathbf{v} = \begin{cases} 0 \\ 0 \\ \hat{\mathbf{e}}_z \end{cases}$$

$$\begin{cases} \mathbf{t} = \frac{1}{\sqrt{2}} (\hat{\mathbf{e}}_z + [\bar{u}] \hat{\mathbf{e}}_x) \\ \mathbf{b} = (\hat{\mathbf{e}}_z \times [\bar{u}] \hat{\mathbf{e}}_x) = [\bar{u}] \hat{\mathbf{e}}_y \\ \mathbf{p} = \frac{1}{\sqrt{2}} (\hat{\mathbf{e}}_z - [\bar{u}] \hat{\mathbf{e}}_x) \end{cases}$$



referred to principal axes

$$\mathbf{M} = \begin{pmatrix} M_0 & 0 & 0 \\ 0 & 0 & 0 \\ 0 & 0 & -M_0 \end{pmatrix}$$



GF for double couple



An important case to consider in detail is the radiation pattern expected when the source is a double-couple. The result for a moment time function $M_0(t)$ is:

$$\begin{aligned}
u = & \frac{A^{NF}}{4\pi\rho|\mathbf{x}|^4} \int_{|\mathbf{x}|/\alpha}^{|\mathbf{x}|/\beta} \tau M_0(t - \tau) d\tau + \\
& + \frac{A_P^{IF}}{4\pi\rho\alpha^2|\mathbf{x}|^2} M_0\left(t - \frac{|\mathbf{x}|}{\alpha}\right) - \frac{A_S^{IF}}{4\pi\rho\beta^2|\mathbf{x}|^2} M_0\left(t - \frac{|\mathbf{x}|}{\beta}\right) + \\
& + \frac{A_P^{FF}}{4\pi\rho\alpha^3|\mathbf{x}|} \dot{M}_0\left(t - \frac{|\mathbf{x}|}{\alpha}\right) - \frac{A_S^{FF}}{4\pi\rho\beta^3|\mathbf{x}|} \dot{M}_0\left(t - \frac{|\mathbf{x}|}{\beta}\right)
\end{aligned}$$

$$A^{NF} = 9\sin 2\theta \cos \phi \hat{\mathbf{r}} - 6(\cos 2\theta \cos \phi \hat{\boldsymbol{\theta}} - \cos \theta \sin \phi \hat{\boldsymbol{\phi}})$$

Near field term

$$A_P^{IF} = 4\sin 2\theta \cos \phi \hat{\mathbf{r}} - 2(\cos 2\theta \cos \phi \hat{\boldsymbol{\theta}} - \cos \theta \sin \phi \hat{\boldsymbol{\phi}})$$

Intermediate field term

$$A_S^{IF} = -3\sin 2\theta \cos \phi \hat{\mathbf{r}} + 3(\cos 2\theta \cos \phi \hat{\boldsymbol{\theta}} - \cos \theta \sin \phi \hat{\boldsymbol{\phi}})$$

$$A_P^{FF} = \sin 2\theta \cos \phi \hat{\mathbf{r}}$$

Far field term

$$A_S^{FF} = \cos 2\theta \cos \phi \hat{\boldsymbol{\theta}} - \cos \theta \sin \phi \hat{\boldsymbol{\phi}}$$



Faulting and Seismograms



- The nature of faulting affects the amplitudes and shapes of seismic waves (this allows us to use seismograms to study the faulting).
- We call the variation in wave amplitude, due to the source, with direction (i.e. angular) the **radiation pattern**.



Far field for a point DC point source



From the representation theorem we have: $u_n(\mathbf{x},t) = M_{pq} * G_{np,q}$
 that, in the far field and in a spherical coordinate system becomes:

$$u(\mathbf{x},t) = \frac{1}{4\pi\rho\alpha^3} (\sin 2\theta \cos \phi \hat{\mathbf{r}}) \frac{\dot{M}(t - r/\alpha)}{r} +$$

$$\frac{1}{4\pi\rho\beta^3} (\cos 2\theta \cos \phi \hat{\boldsymbol{\theta}} - \cos \theta \sin \phi \hat{\boldsymbol{\phi}}) \frac{\dot{M}(t - r/\beta)}{r}$$

and both P and S radiation fields are proportional to the time derivative of the moment function (moment rate).
 If the moment function is a ramp of duration τ (**rise time**), the propagating disturbance in the far-field will be a **boxcar**, with the same duration, and whose amplitude is varying depending on the radiation pattern.



FIGURE 8.21 Far-field P- and S-wave displacements are proportional to $\dot{M}(t)$, the time derivative of the moment function $M(t) = \mu A(t)D(t)$. Simple step and ramp moment functions generate far-field impulses or boxcar ground motions.



P-wave radiation amplitude patterns:

$$u_r = \frac{1}{4\pi\rho\alpha^3r} \dot{M}(t - r/\alpha) \sin 2\theta \cos \phi.$$

$\frac{1}{4\pi\rho\alpha^3r}$ = amplitude term, with geometric spreading

$\sin 2\theta \cos \phi$ = *P*-wave radiation pattern (4-lobed)

$\dot{M}(t - r/\alpha)$ = source time function

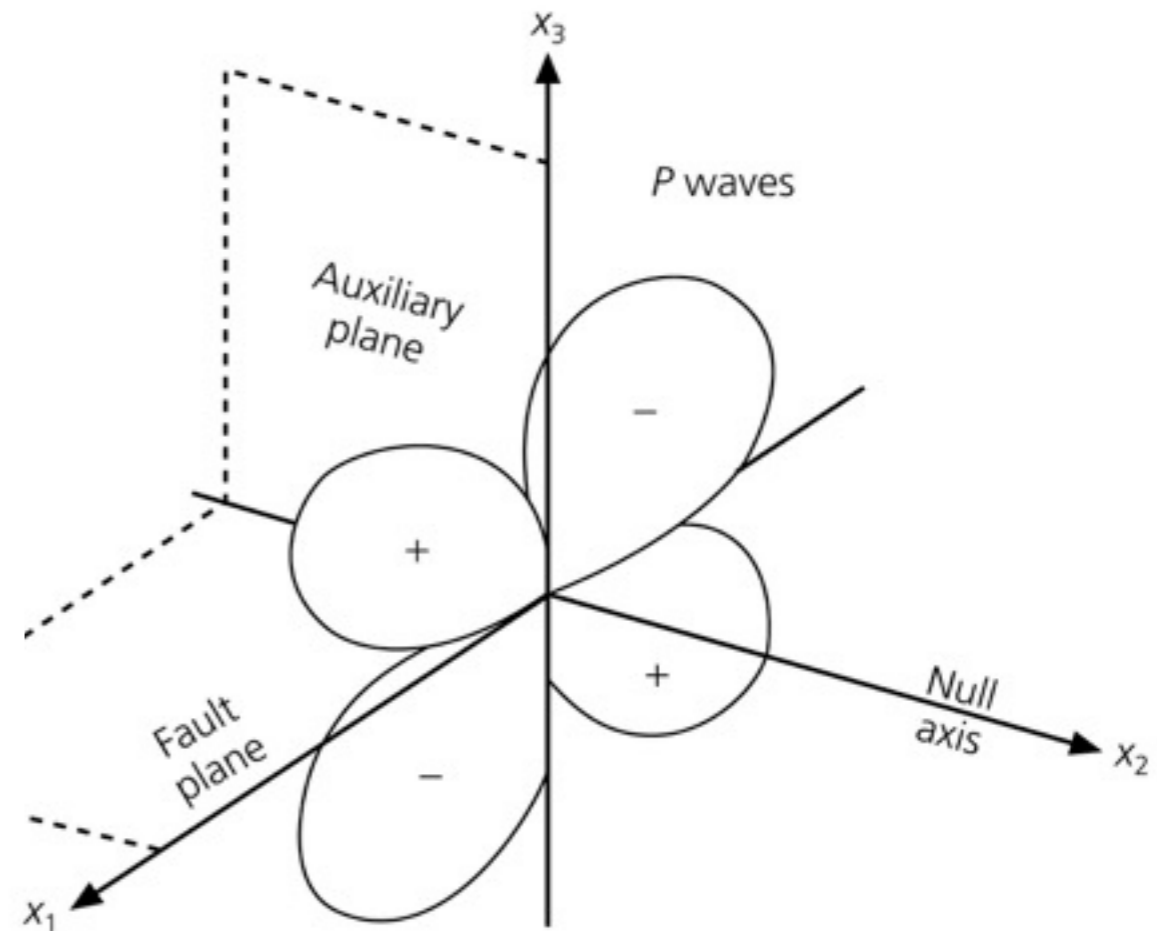
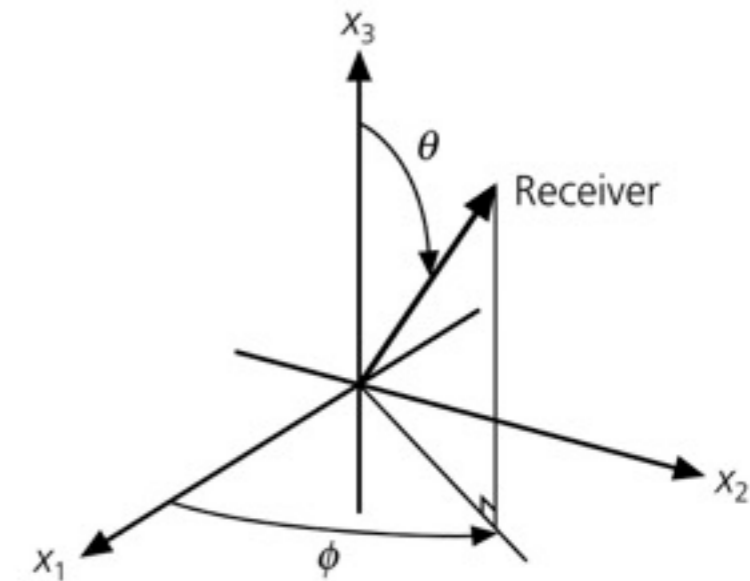
\dot{M} is the time derivative of the seismic moment function,

$$M(t) = \mu D(t)S(t)$$

$D(t)$ = slip history

$S(t)$ = fault area history

: Body-wave radiation patterns for a double couple source.





S-wave radiation amplitude patterns:

$$u_{\theta} = \frac{1}{4\pi\rho\beta^3r} \dot{M}(t - r/\beta) \cos 2\theta \cos \phi$$

$$u_{\phi} = \frac{1}{4\pi\rho\beta^3r} \dot{M}(t - r/\beta) (-\cos \theta \sin \phi)$$

Why are *S* waves usually larger than *P* waves?

These equations predict an average ratio of about α^3/β^3 or about 5.

Figure 4.2-6: Body-wave radiation patterns for a double couple source.

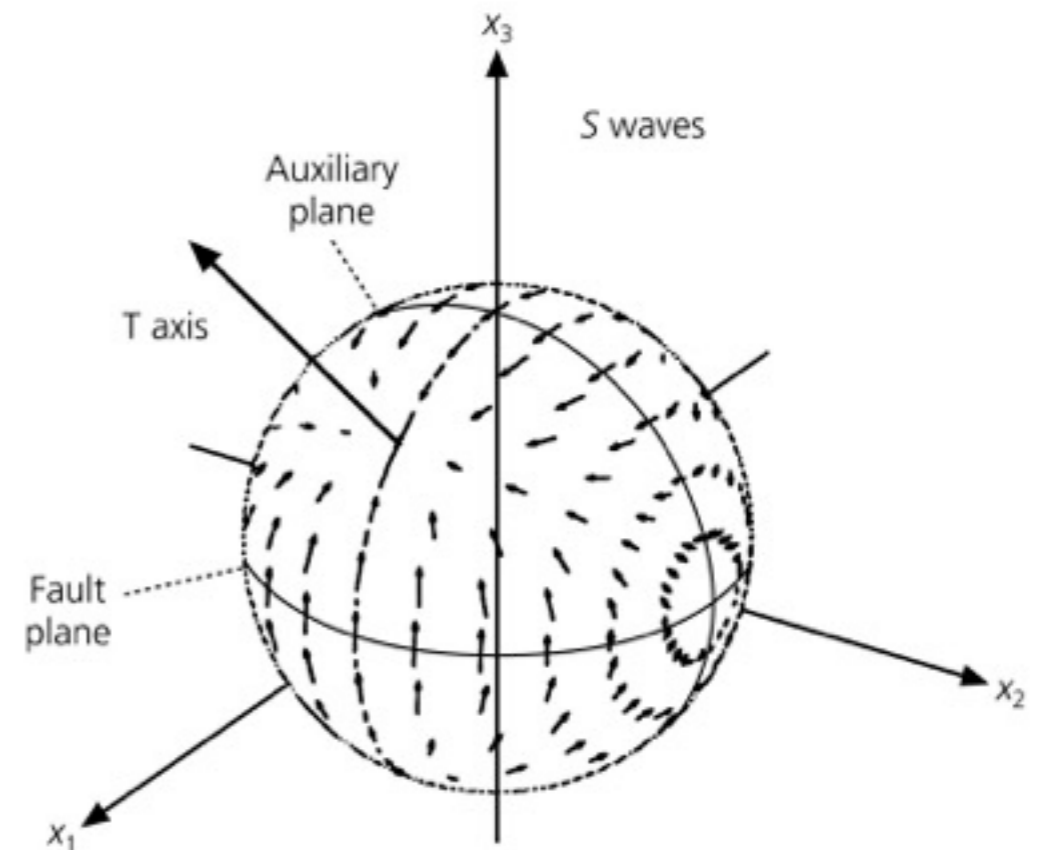
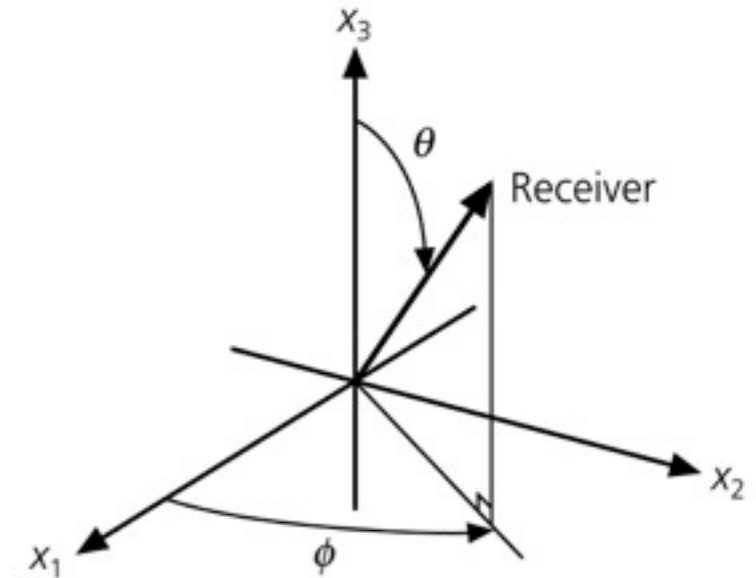
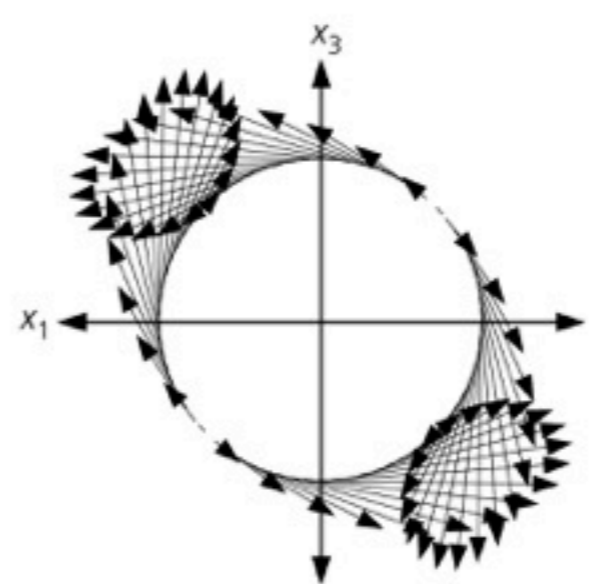
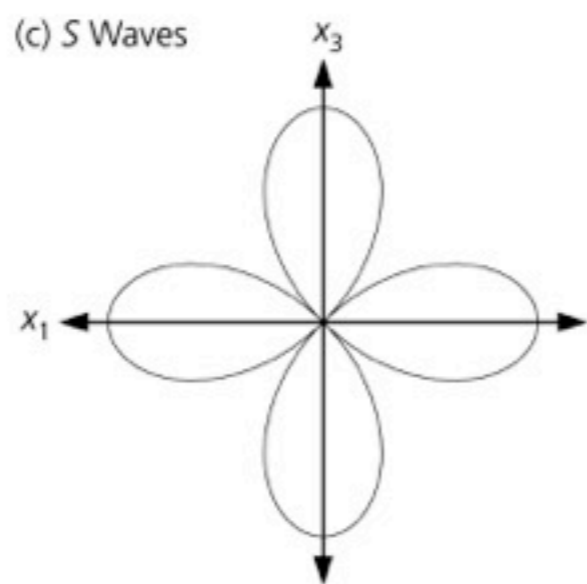
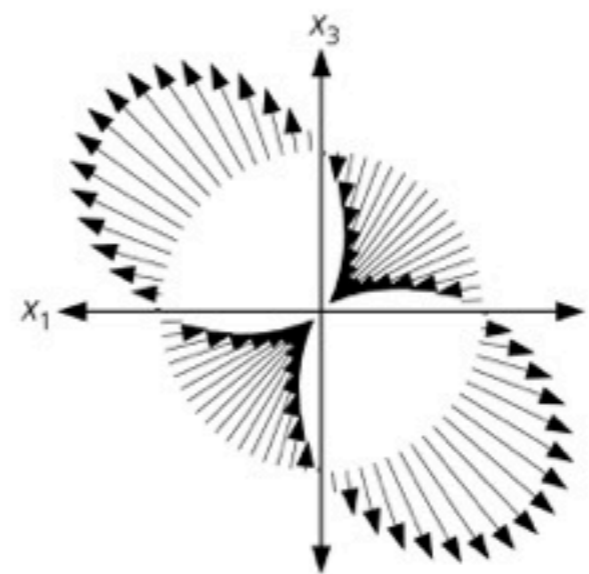
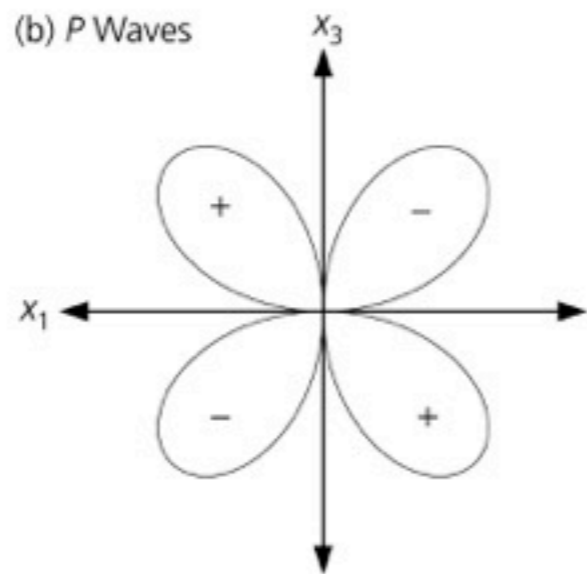
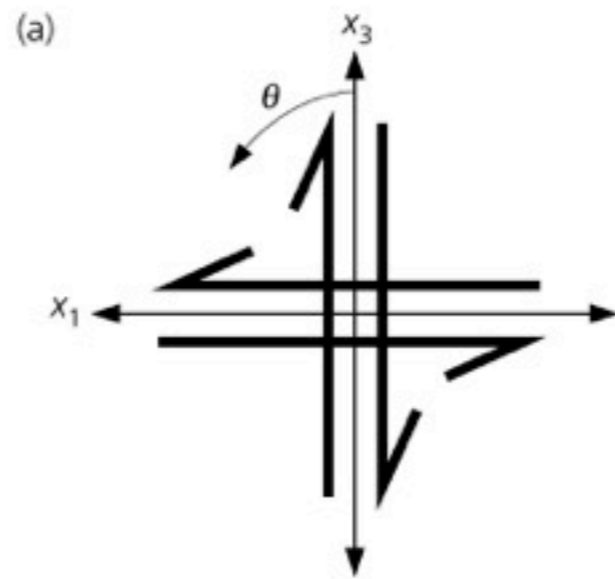




Figure 4.2-7: *P* and *S* radiation amplitude patterns.

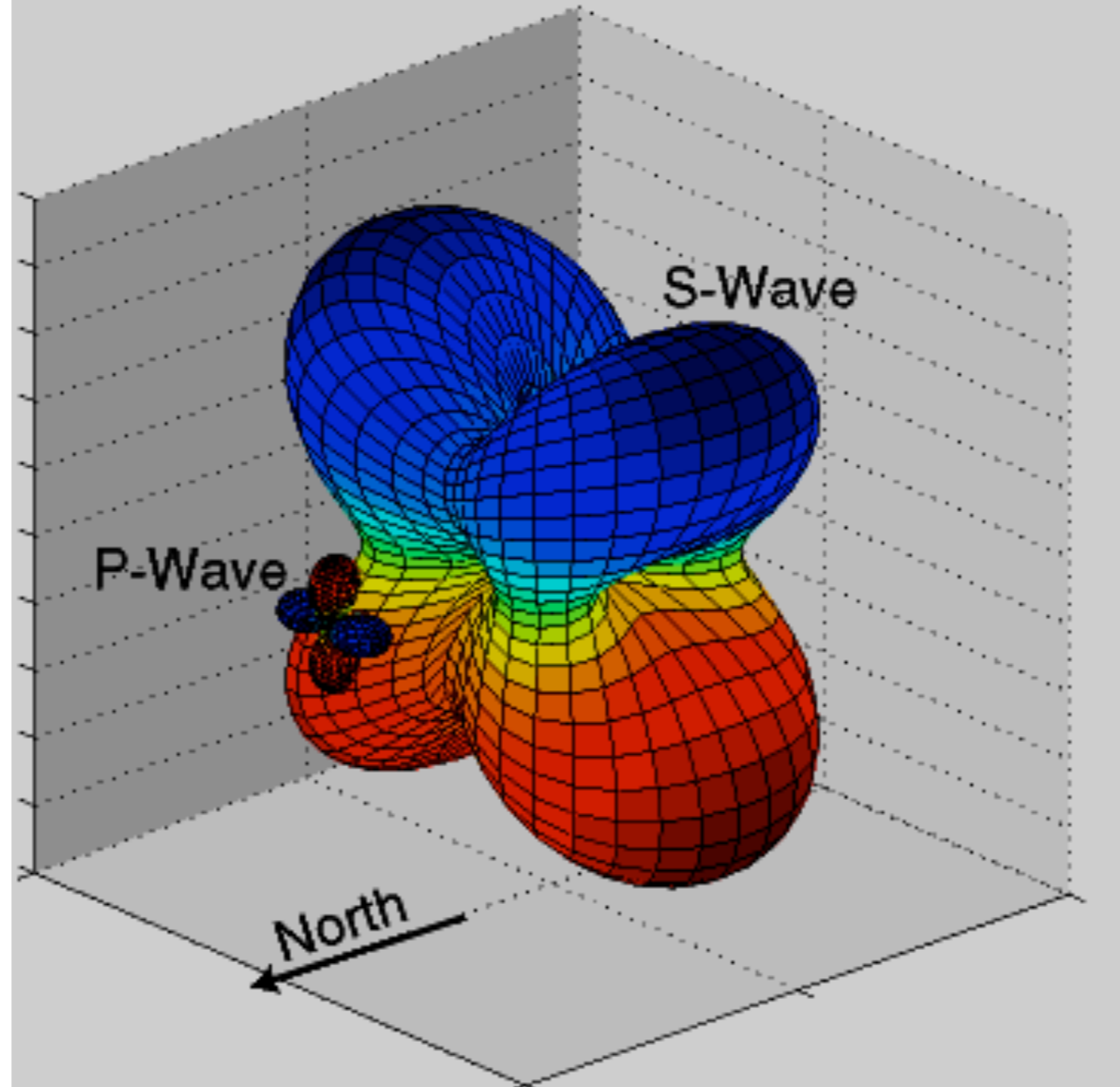




Radiation Patterns in 3D

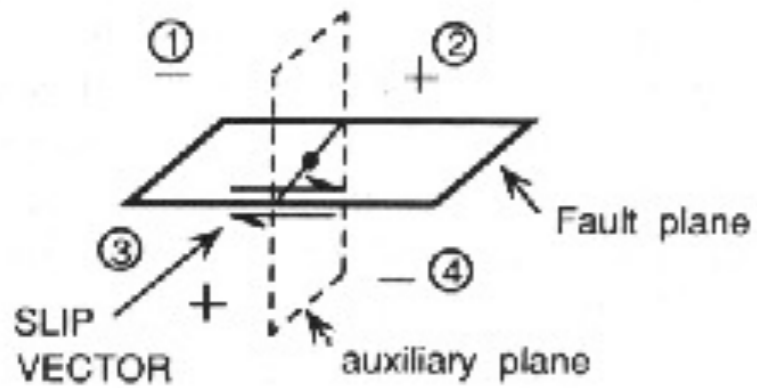


Radiation Patterns of P and S waves
for a 45° Dipping Fault with a Strike Due North



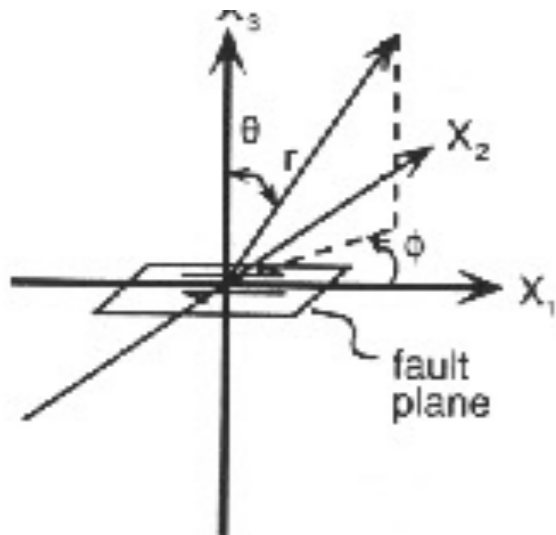


Radiation from shear dislocation

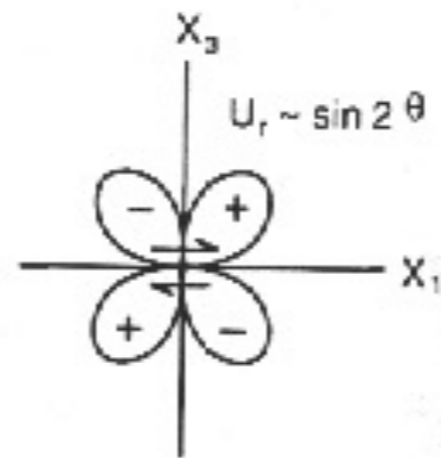


Fault plane and auxiliary plane and sense of initial P-wave motion.

a



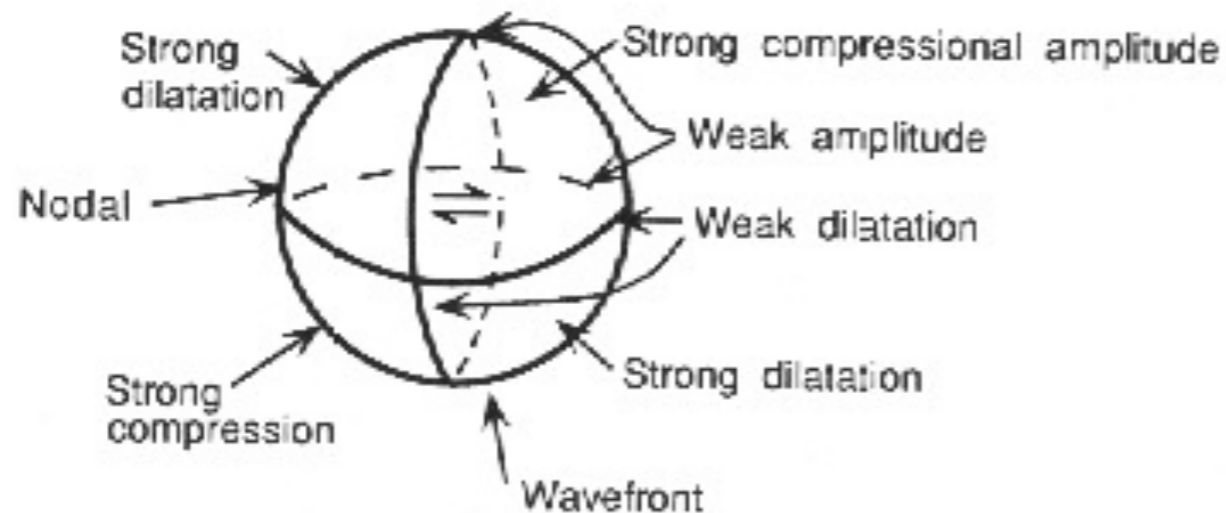
b



a) Coordinates parallel or perpendicular to fault plane with one axis along the slip direction.

b) radiation pattern in x-z plane

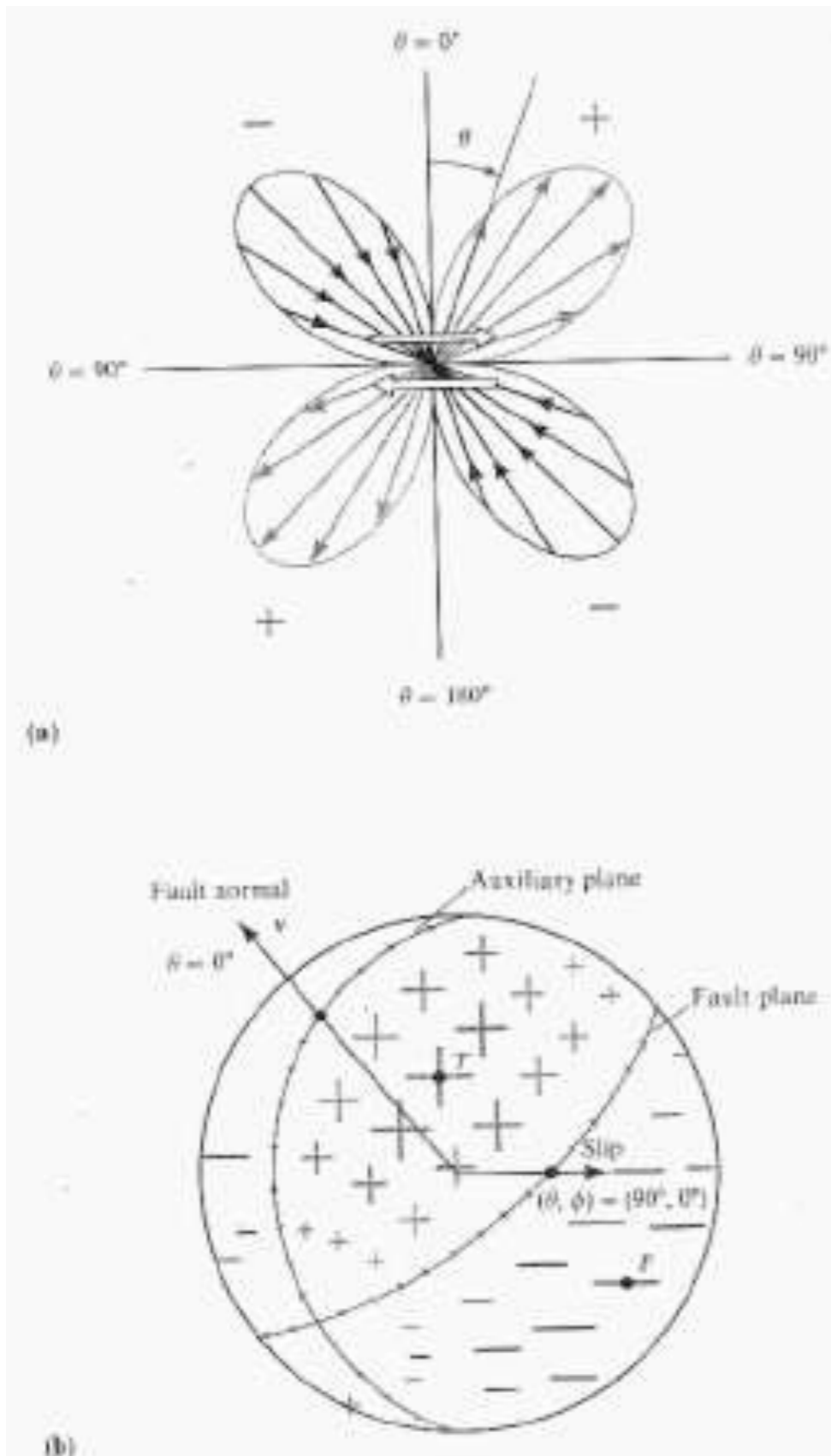
c



c) 3-D variation of P amplitude and polarity of wavefront from a shear dislocation



Double Couple radiation pattern - P waves



Radiation pattern of the radial displacement component (P-wave) due to a double-couple source:

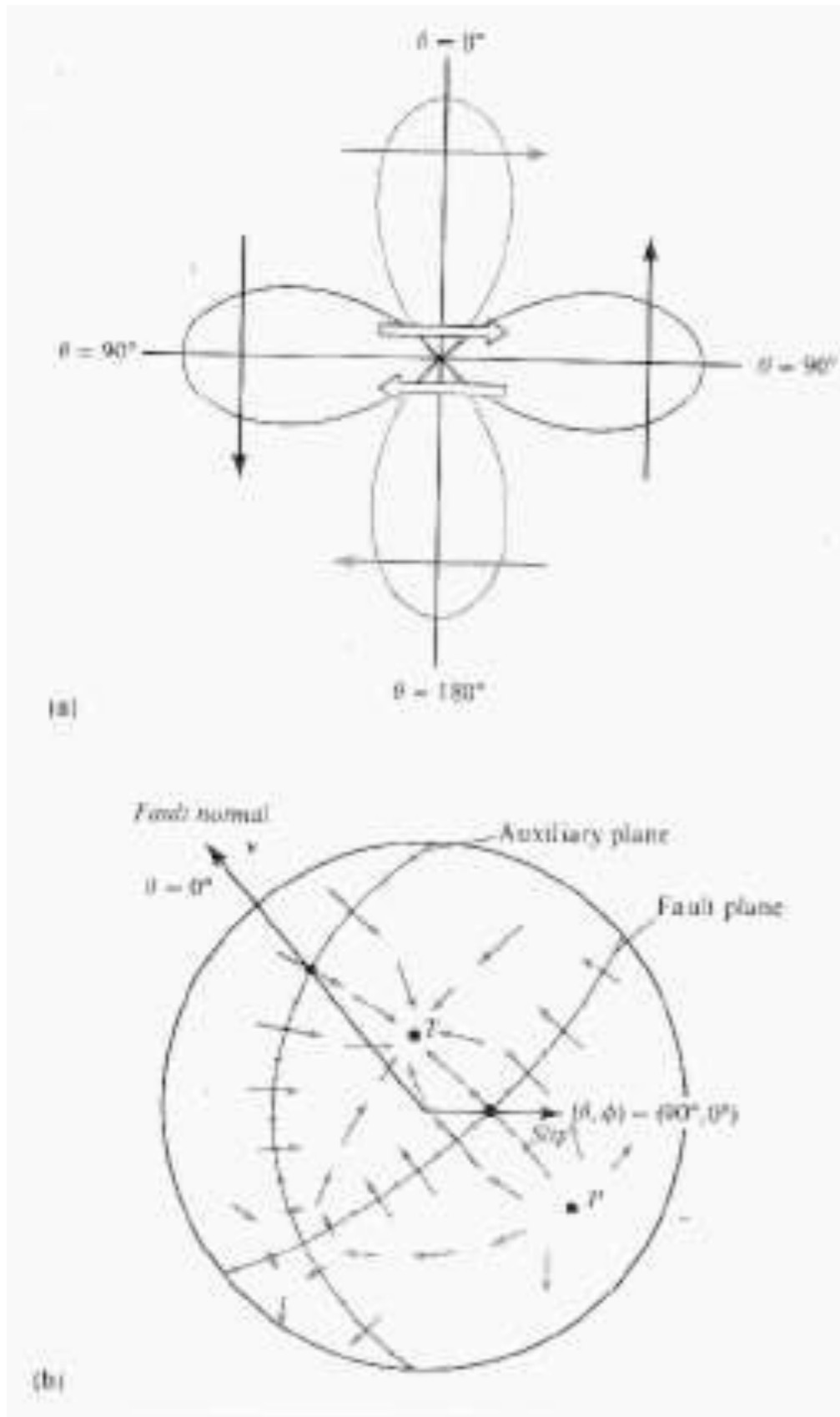
a) for a plane of constant azimuth (with lobe amplitudes proportional to $\sin 2\theta$). The pair of arrows at the center denotes the shear dislocation.

b) over the focal sphere centered on the origin. Plus and minus signs of various sizes denote amplitude variation (with θ and ϕ) of outward and inward directed motions. The fault plane and auxiliary plane are nodal lines on which $\cos\phi \sin 2\theta = 0$.

Note the **alternating quadrants of inward and outward directions**.



Double Couple radiation pattern - S waves



Radiation pattern of the transverse displacement component (S-wave) due to a double-couple source: a) in the plane $\{\phi = 0, \phi = \pi\}$.

Arrows imposed on each lobe show the direction of particle displacement; the pair of arrows in a) at the center denotes the shear dislocation

b) over a sphere centered on the origin. Arrows with varying size and direction indicate the variation of the transverse motions with θ and ϕ . There are no nodal lines but only nodal points where there is zero motion.

Note that the nodal point for transverse motion at $(\theta, \phi) = (45^\circ, 0^\circ)$ at T is a maximum in the pattern for longitudinal motion while the maximum transverse motion (e.g. at $\theta = 0$) occurs on a nodal line for the longitudinal motion.



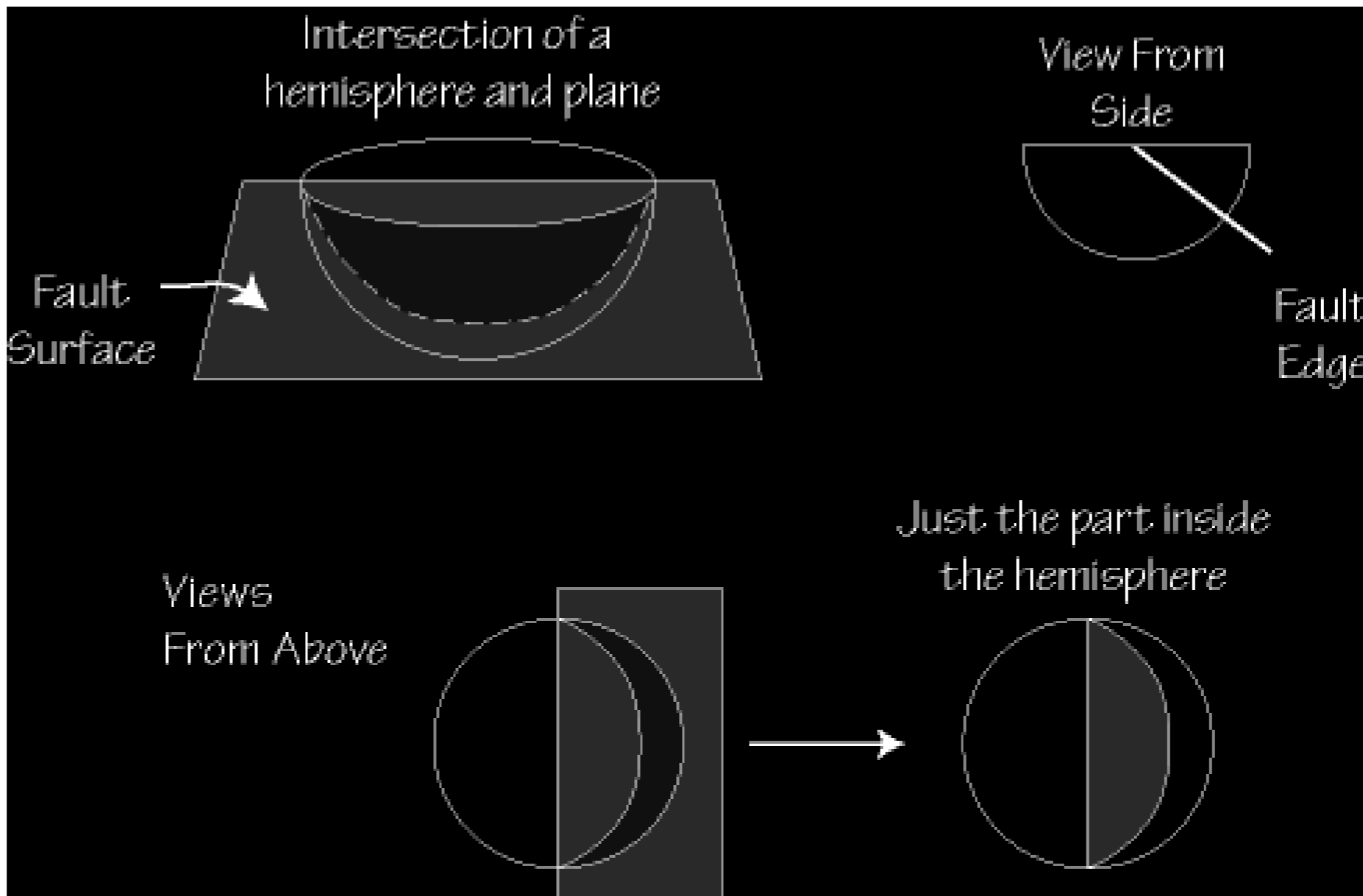
Seismic "Beach Balls"



- We use the radiation patterns of P-waves to construct a graphical representation of earthquake faulting geometry.
- The symbols are called "Focal Mechanisms" or "Beach Balls", and they contain information on the fault orientation and the direction of slip.
- They are:
 - Graphical shorthand for a specific faulting process (strike, dip, slip)
 - Projections of a sphere onto a circle (the lower focal hemisphere)
 - Representations of the first motion of seismic waves.
- When mapping the focal sphere to a circle (beachball) two things happen:
 - Lines (vectors) become points
 - Planes become curved lines



Representing a Plane

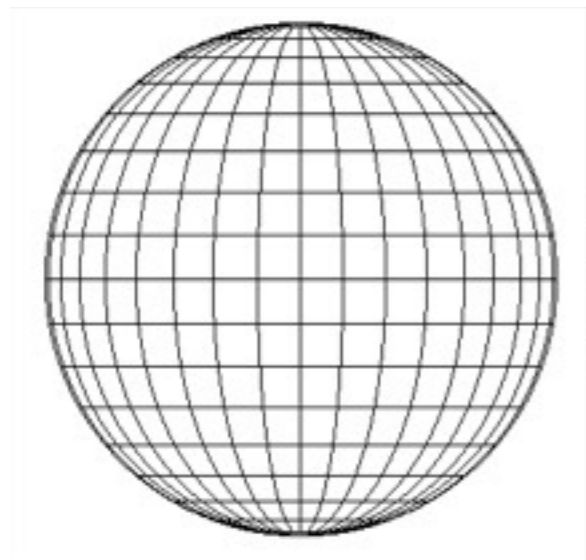




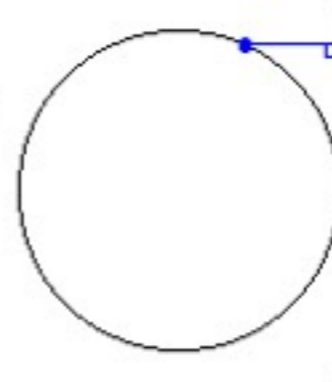
Two steps to understanding



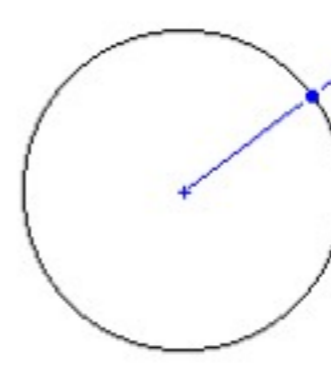
- 1) The stereographic projection
- 2) The geometry of first motions and how this is used to define fault motion.



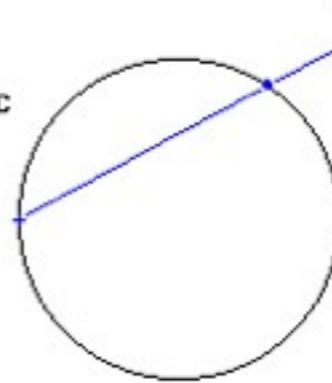
Orthographic



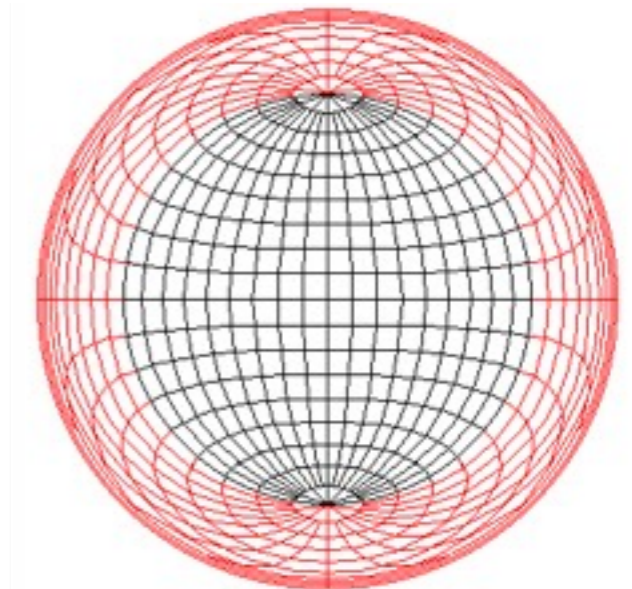
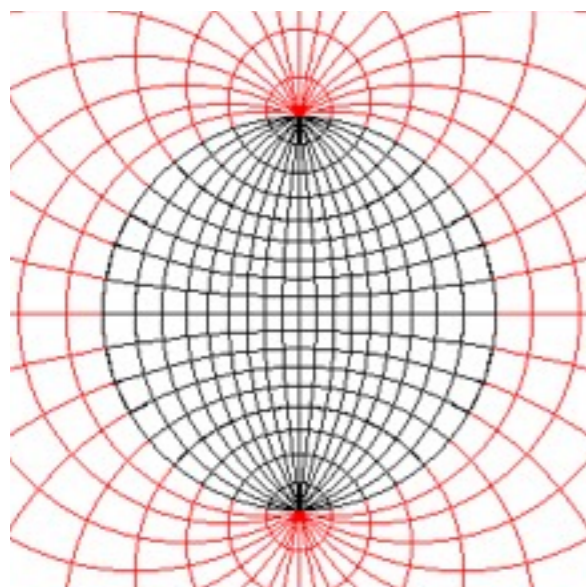
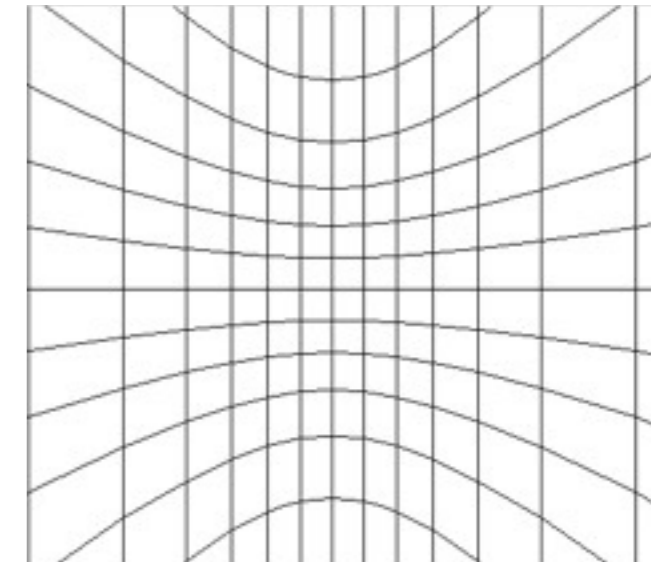
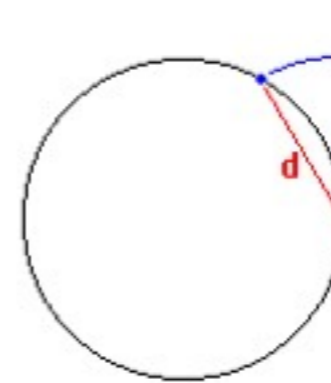
Gnomonic



Stereographic



Equal-Area



Source:USGS

<http://www.uwsp.edu/geo/projects/geoweb/participants/dutch/STRUCTGE/sphproj.htm>

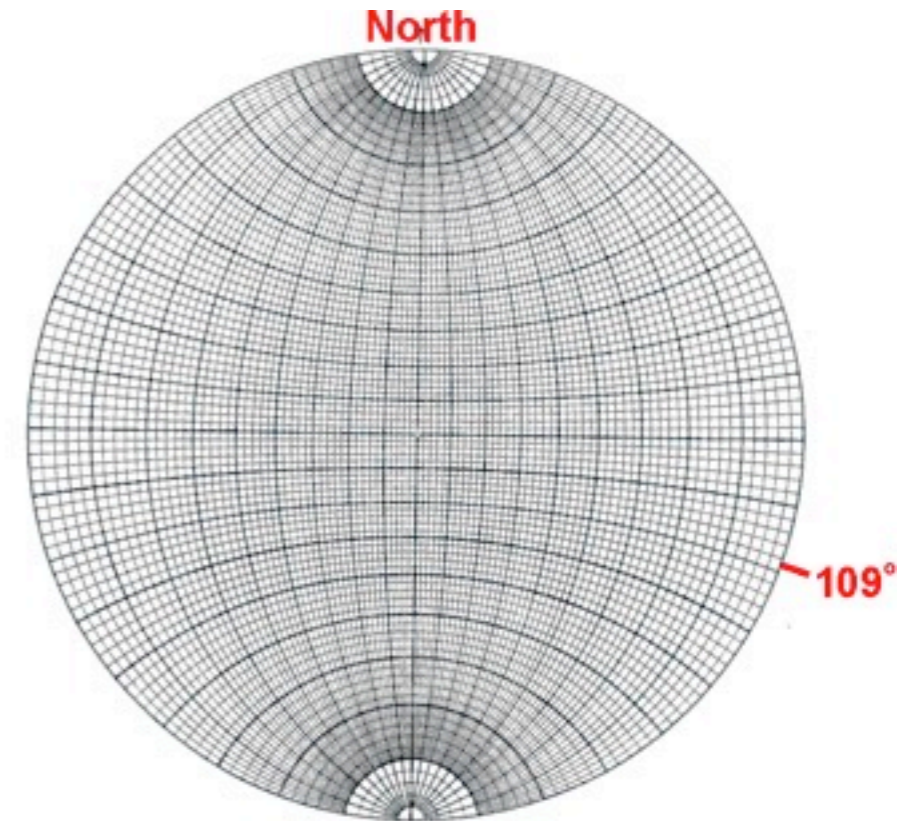
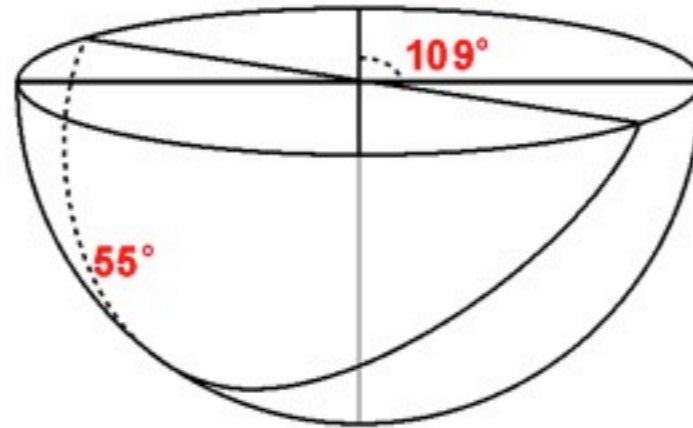


Stereonet

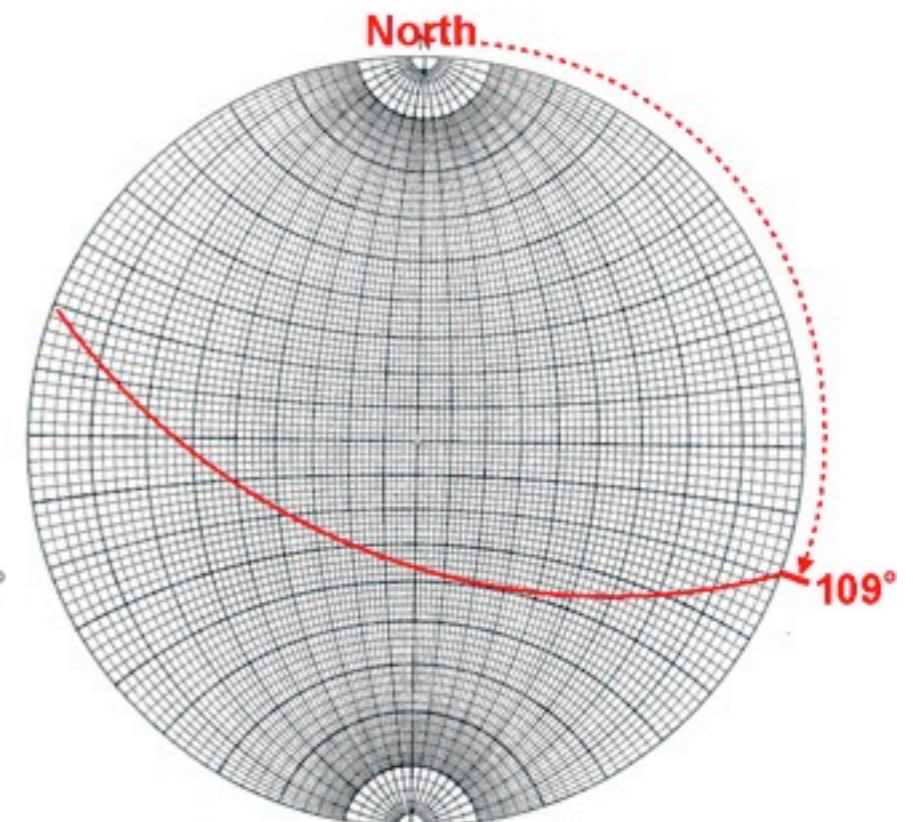
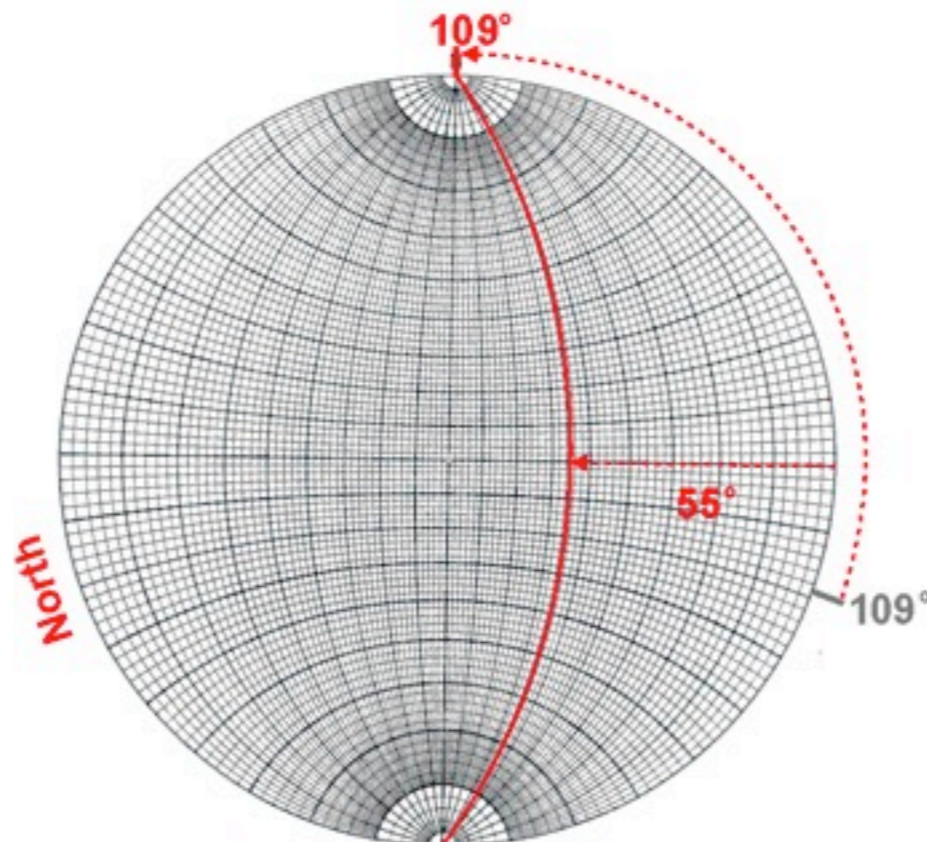


- A template called a stereonet is used to plot data.

Fault strike 109° dip 55° SW



- Example - plotting planes (e.g. faults)



Source:USGS



Figure 4.2-9: Stereonet used to display a hemisphere on a flat surface.

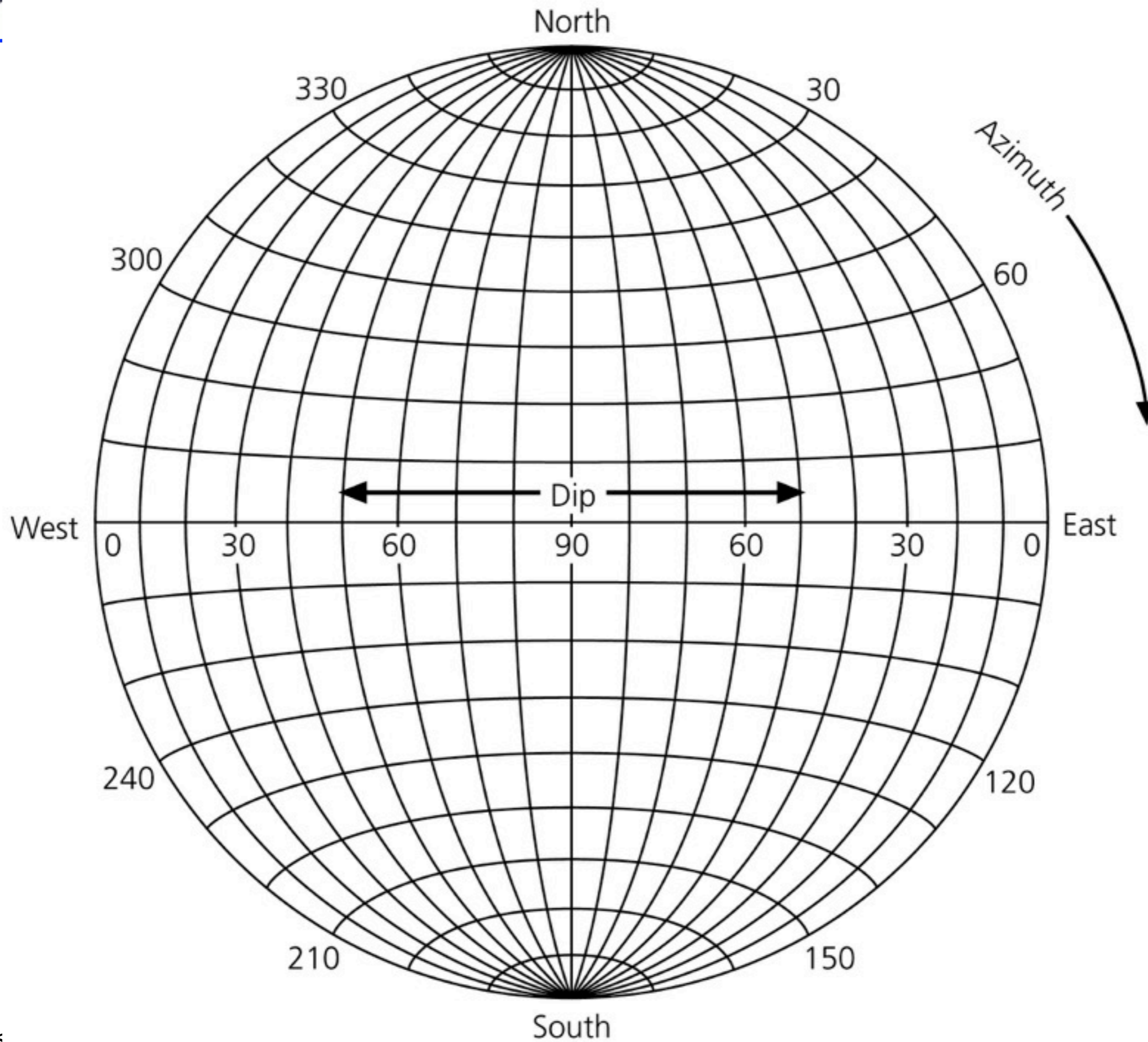




Figure 4.2-10: Example of three planes on a stereonet.

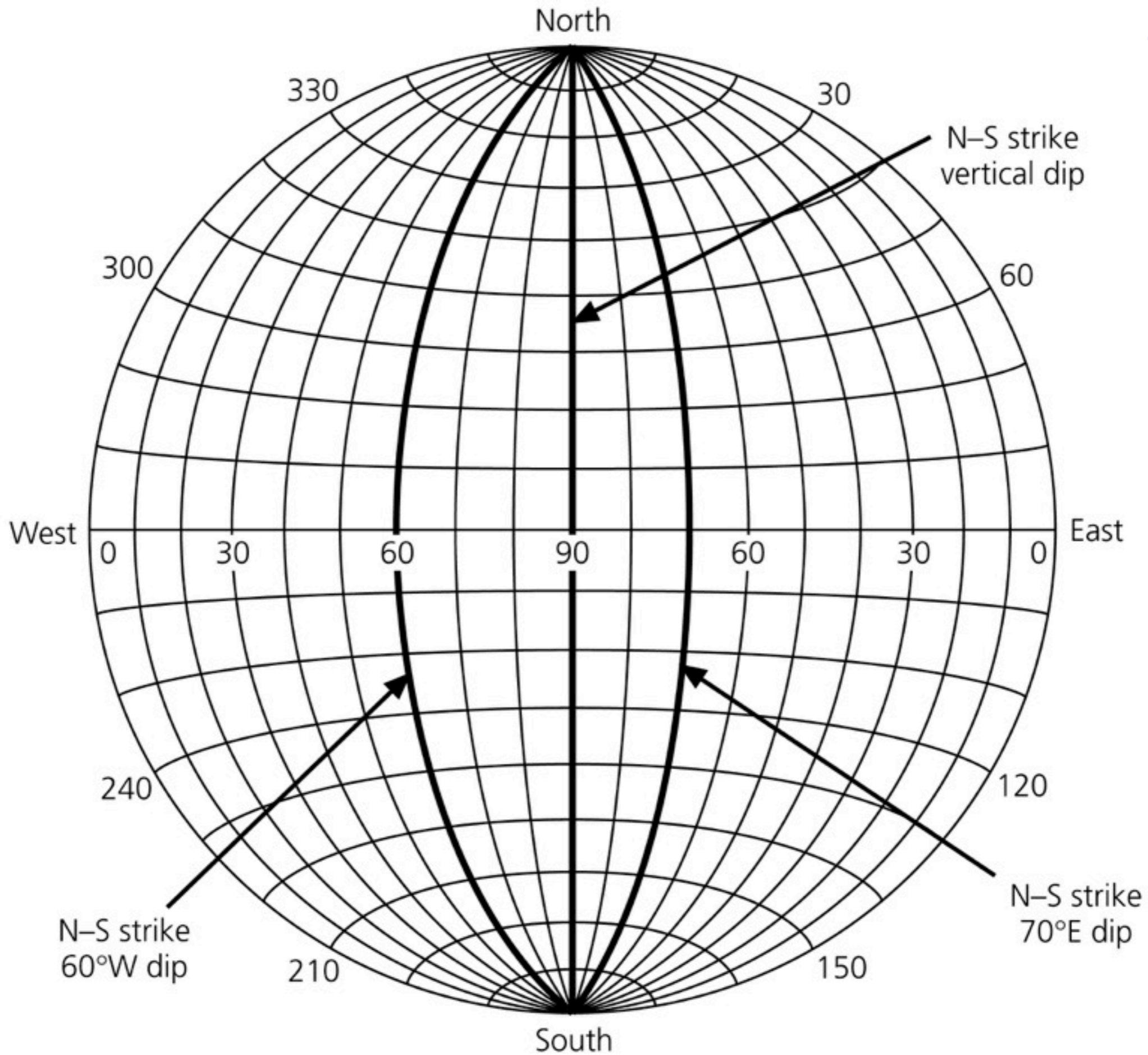




Figure 4.2-11: Example of plotting a plane on a stereonet.

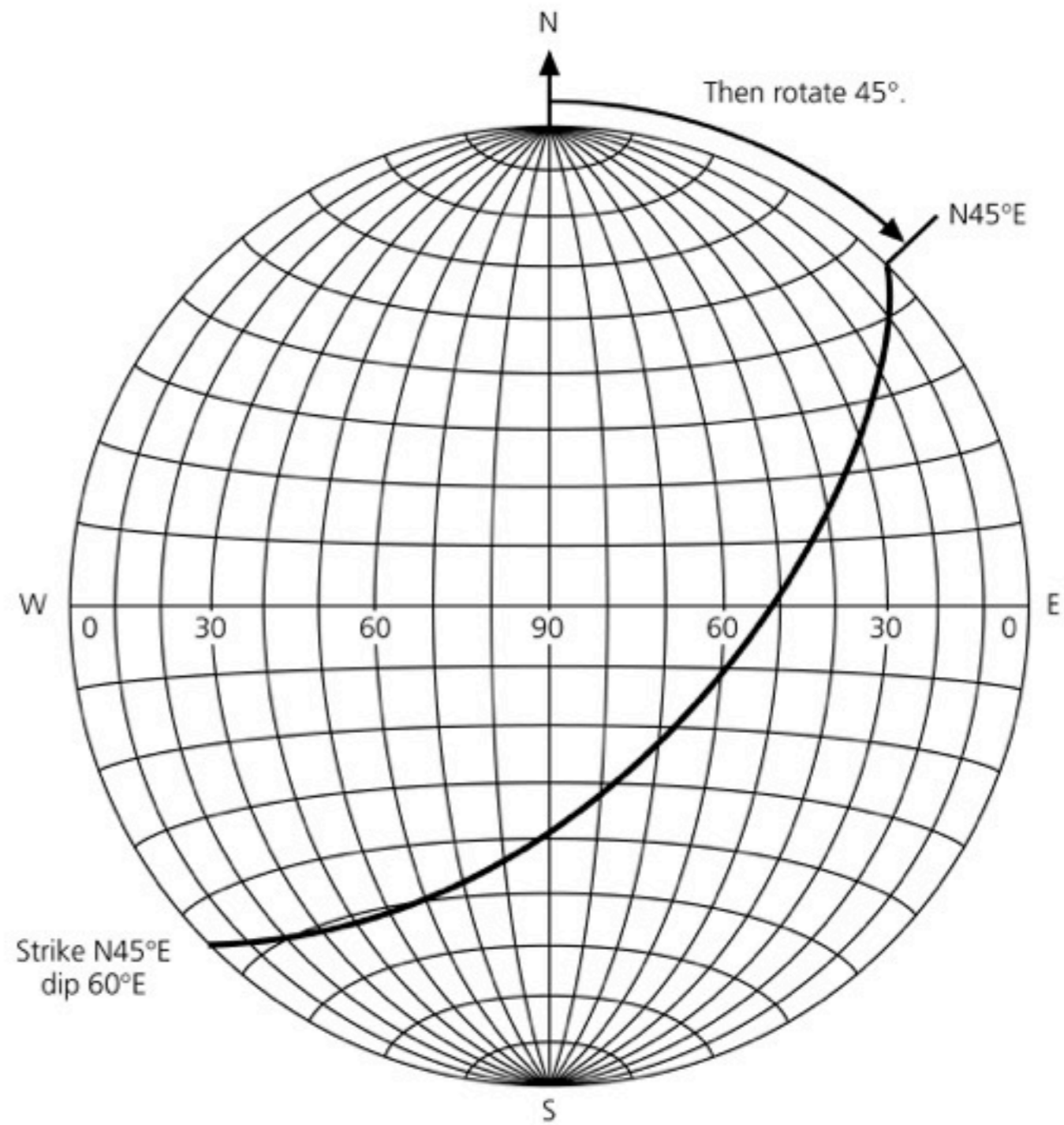
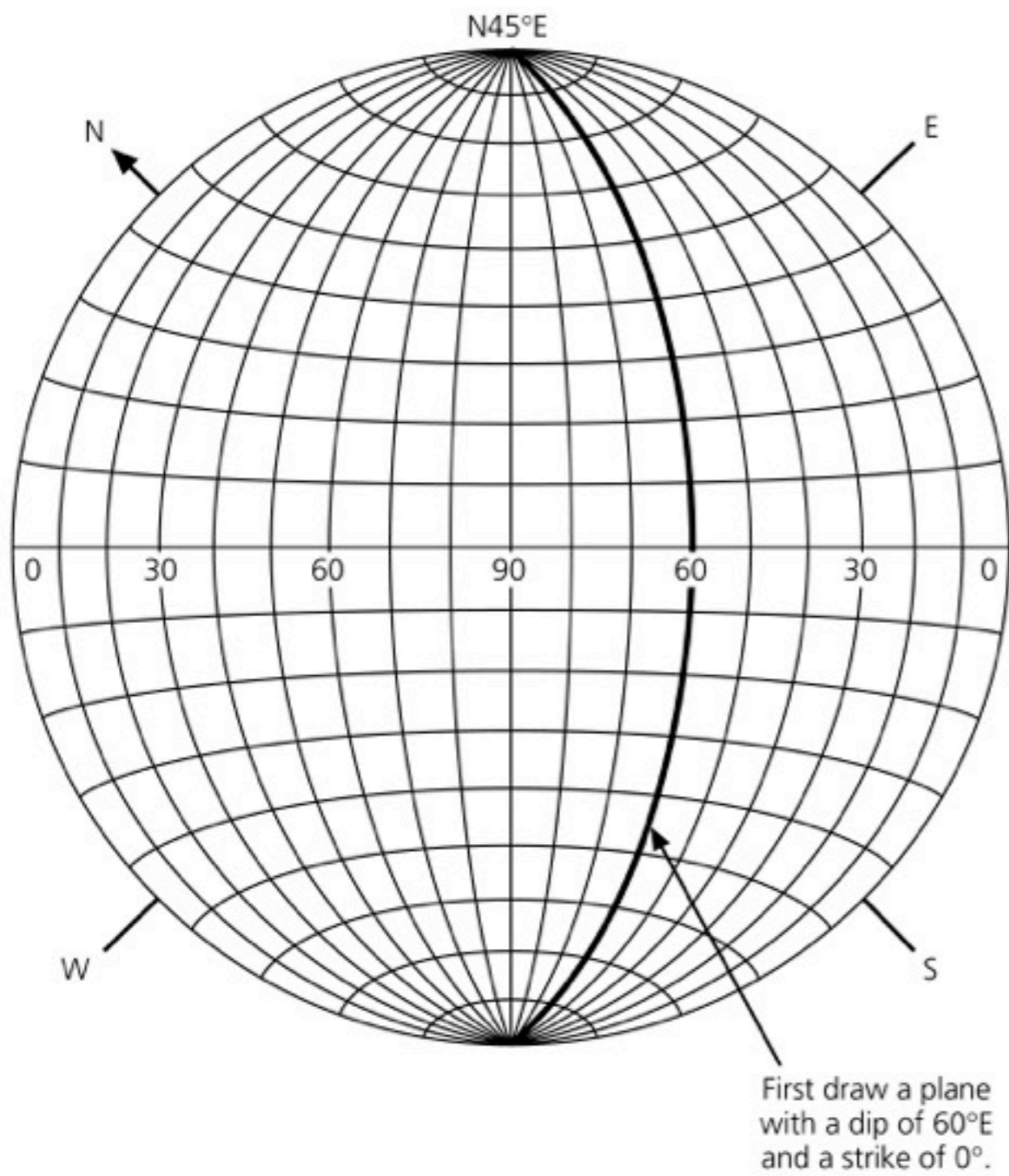
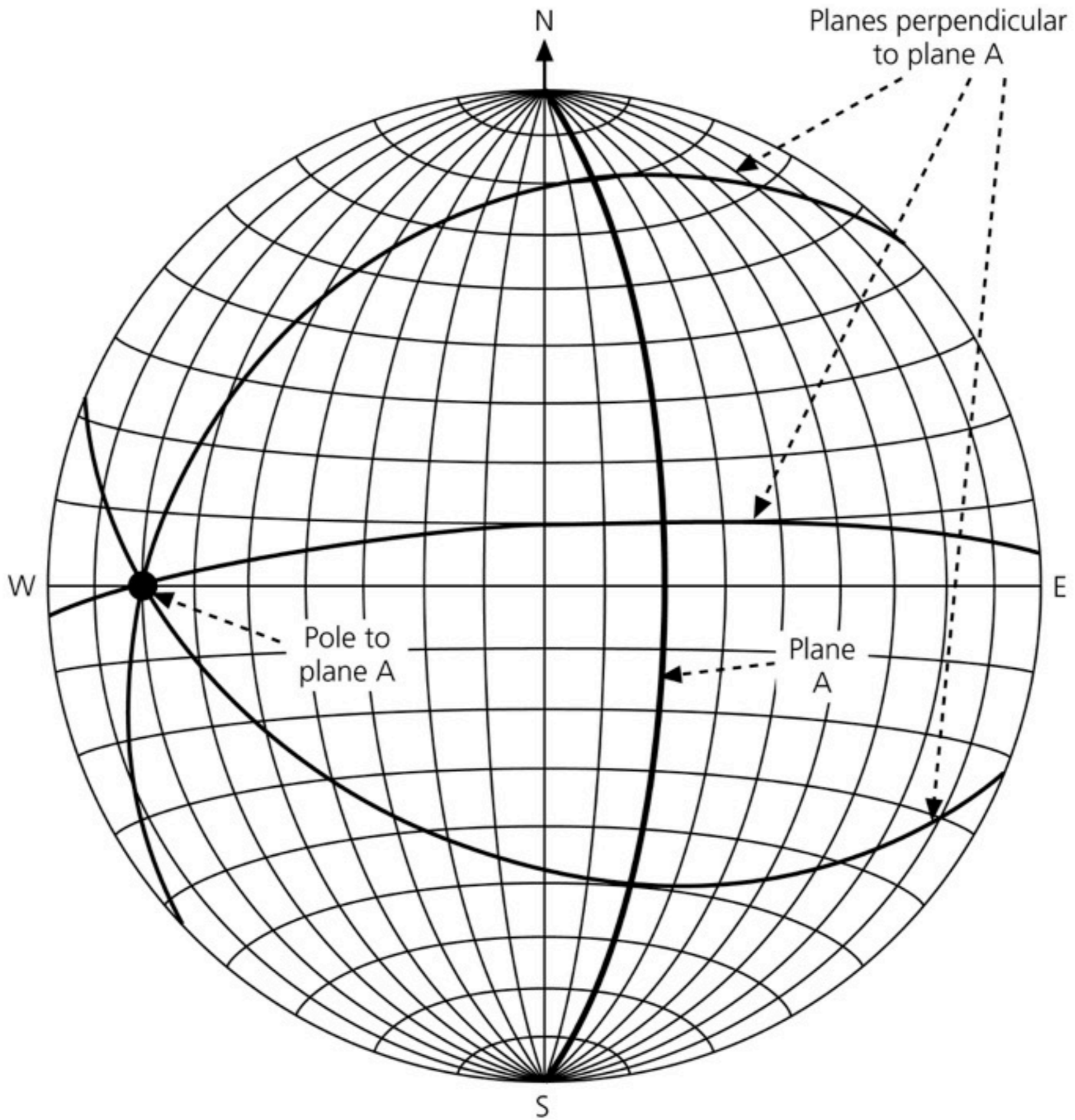




Figure 4.2-12: Example of plotting perpendicular planes on a stereonet.

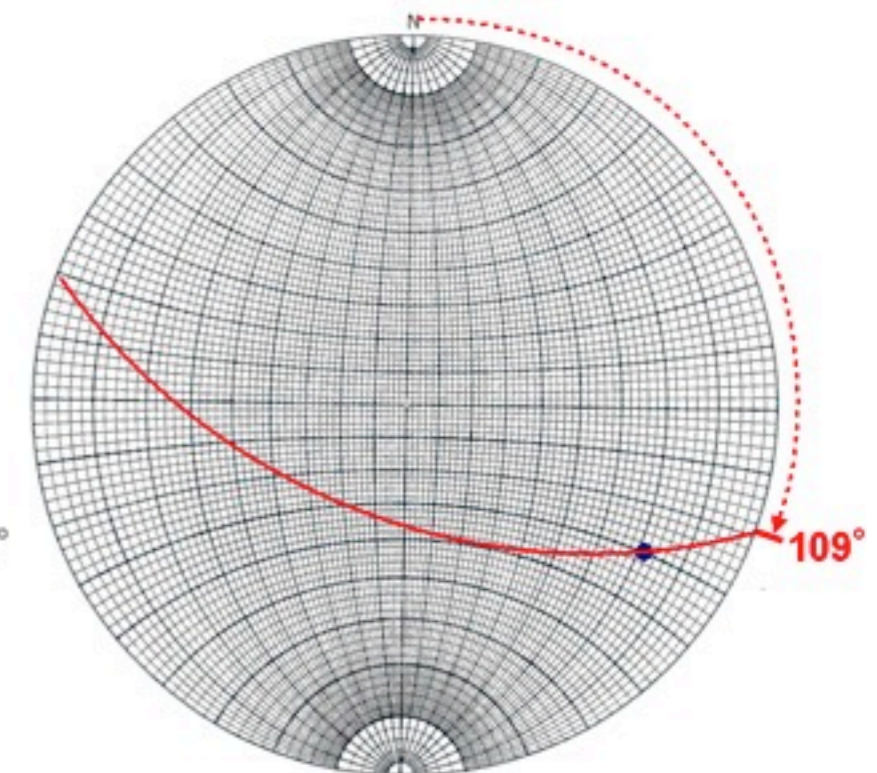
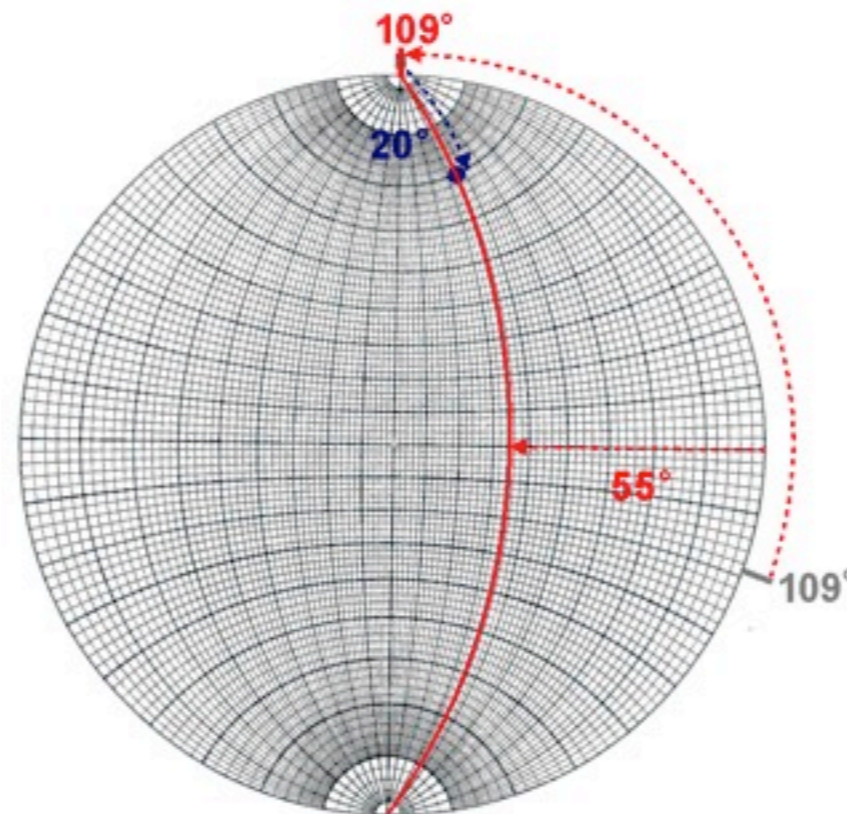
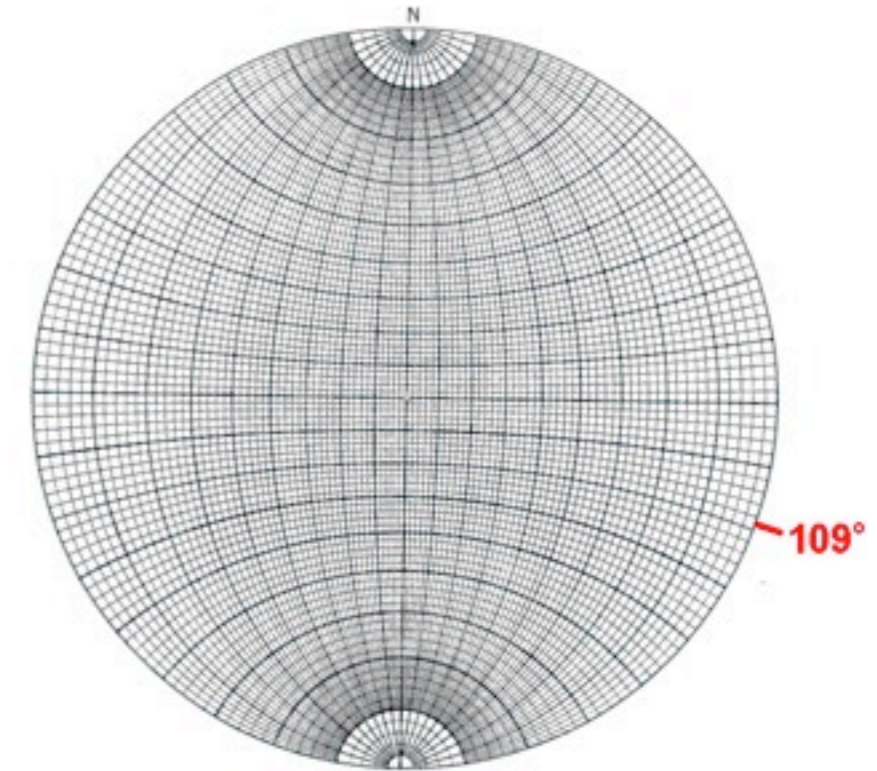
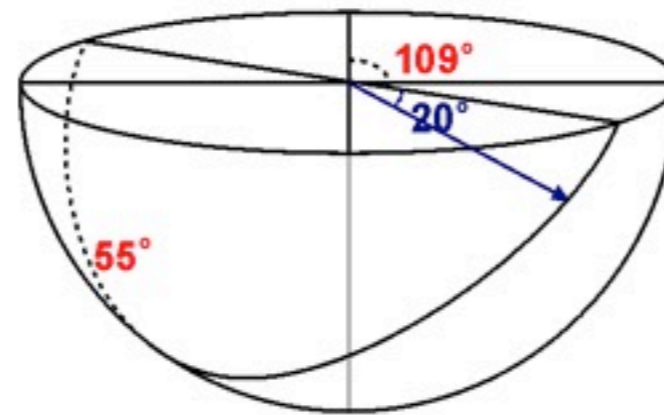




Stereonet



- Example - pitch (or rake) of a line on a plane (e.g. the slip direction on a fault)



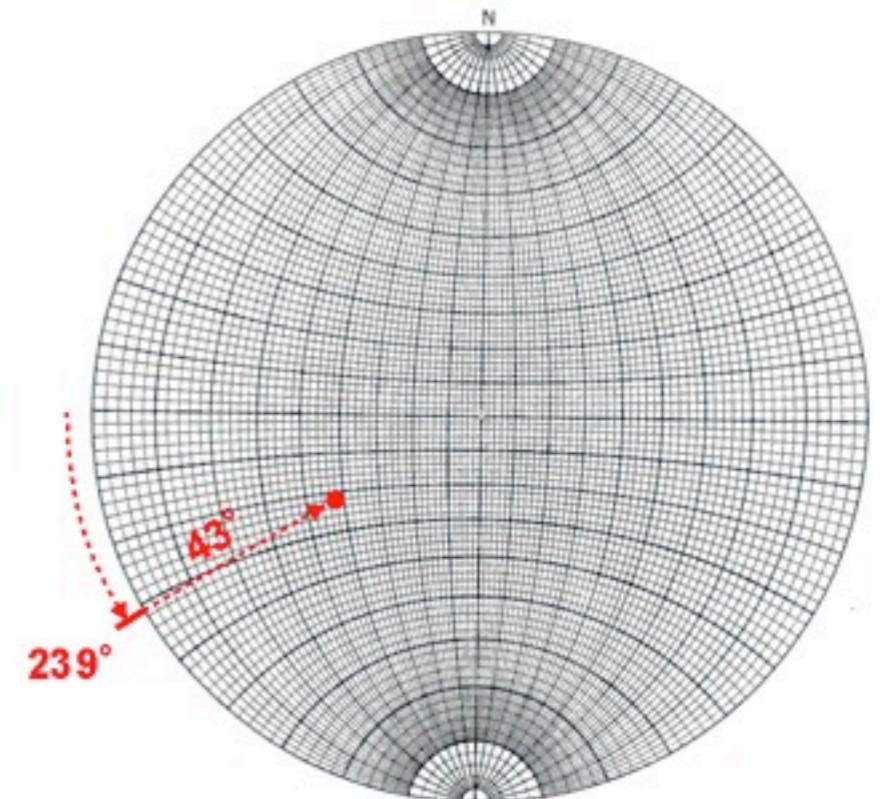
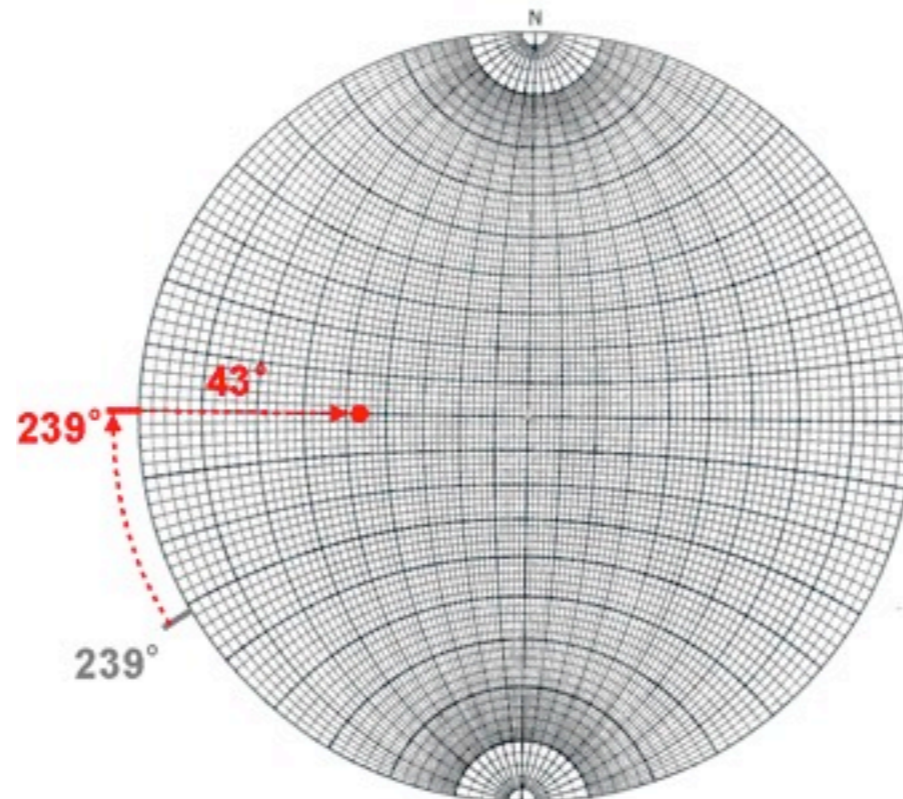
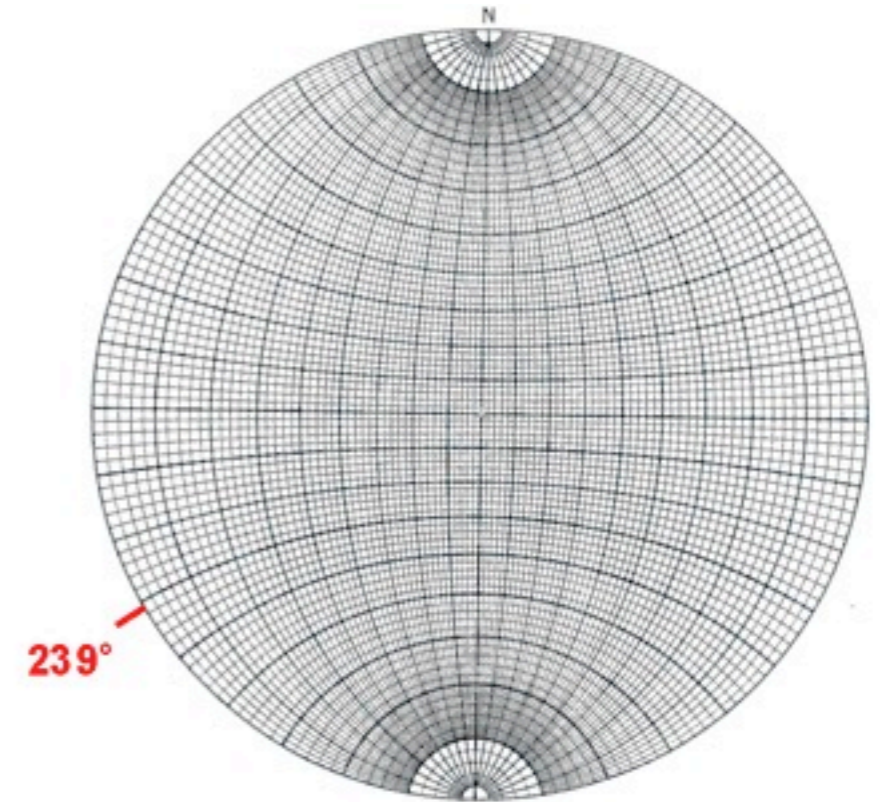
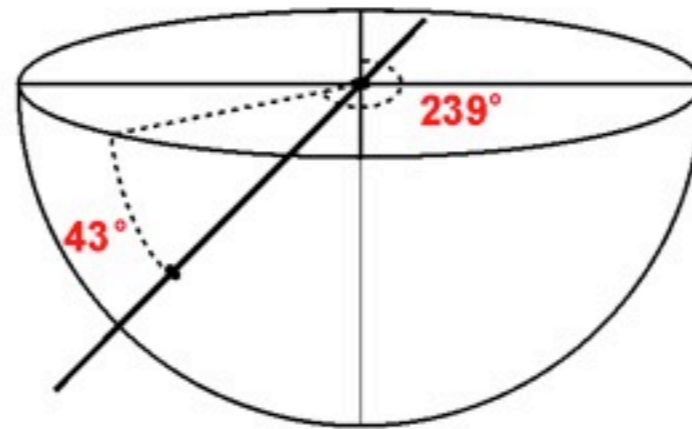
Source:USGS



Stereonet



- Example - plotting lines (e.g. ray paths)



Source:USGS

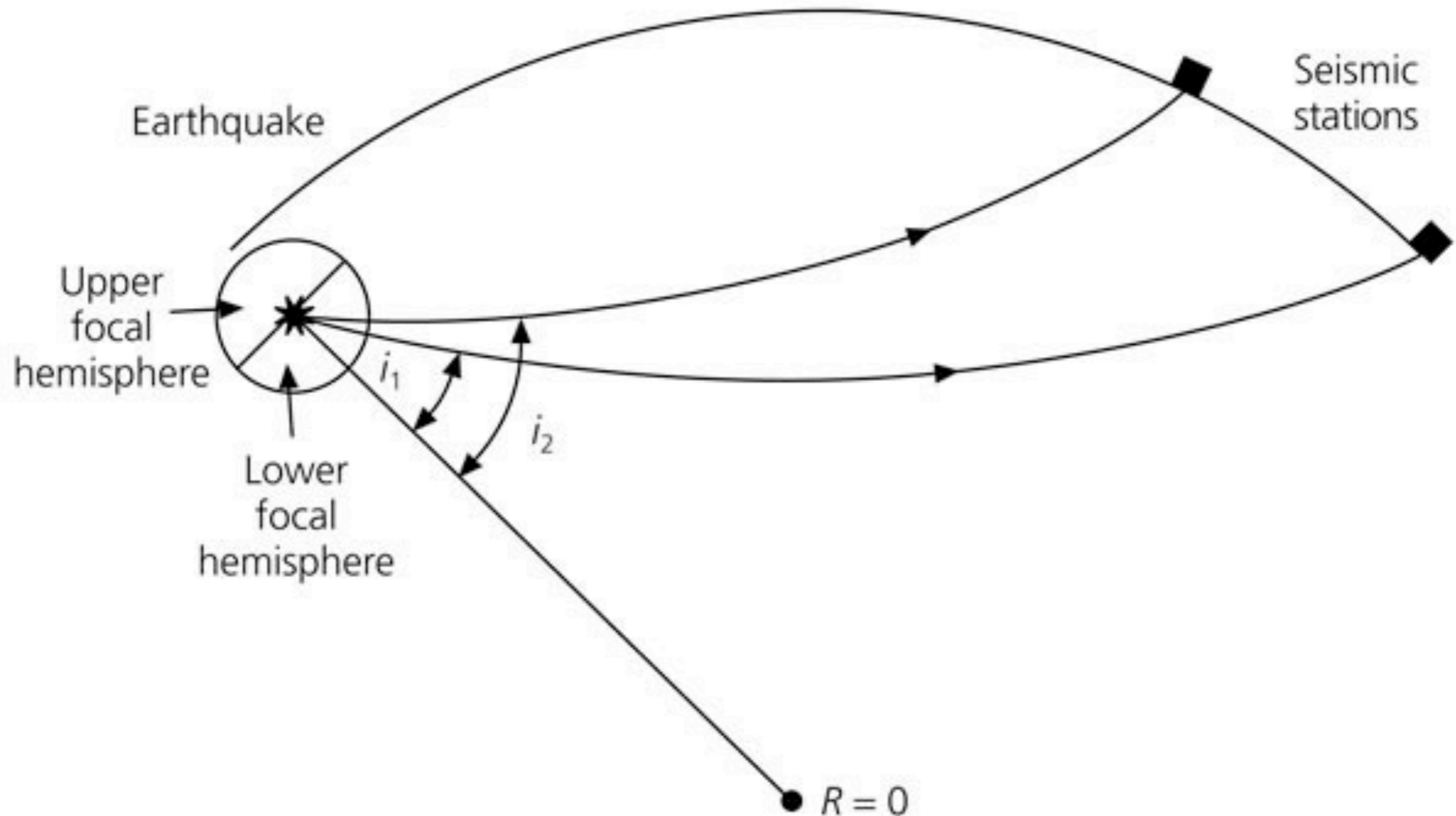


Focal sphere



In order to simplify the analysis, the concept of the "focal sphere" is introduced. The focal sphere is an imaginary sphere drawn around the source region enclosing the fault. If we know the earthquake location and local Earth structure, we can trace rays from the source region to the stations and find the ray take-off angle at the source to a given station.

Figure 4.2-8: Cartoon of the focal sphere.





Take-off angle



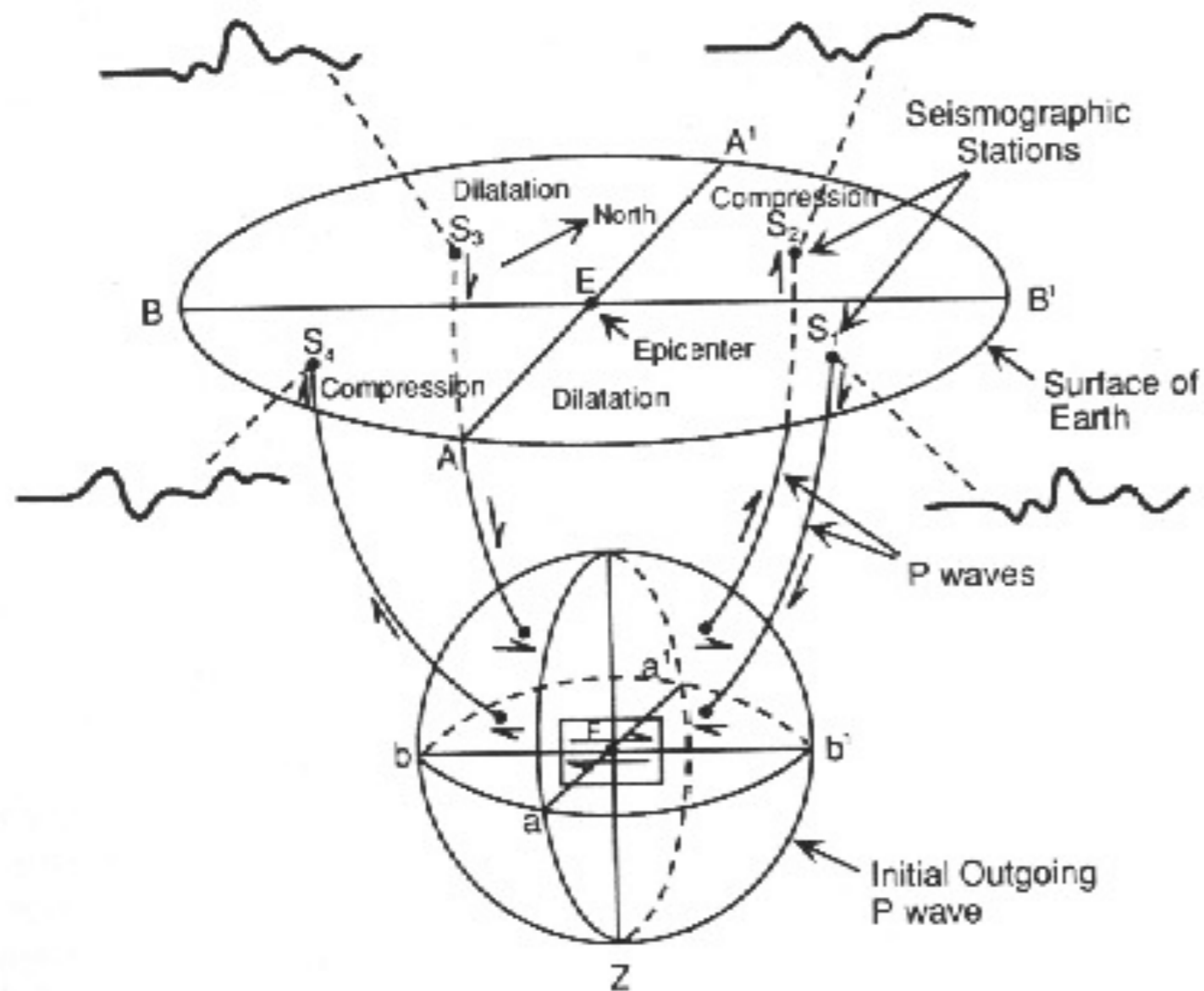
At a given source-receiver, the distance can be determined and from this T and the slope (p) can be found from the travel time tables. For example, the Jeffreys-Bullen travel time tables can be used to obtain p and from this the take-off angle i .

Table 4.2-1: P wave take-off angles for a surface focus earthquake.

Distance (°)	Take-off angle (°)	Distance (°)	Take-off angle (°)	Distance (°)	Take-off angle (°)
21	35	47	25	73	19
23	32	49	24	75	18
25	30	51	24	77	18
27	29	53	23	79	17
29	29	55	23	81	17
31	29	57	23	83	16
33	28	59	22	85	16
35	28	61	22	87	15
37	27	63	21	89	15
39	29	65	21	91	15
41	26	67	20	93	14
43	26	69	20	95	14
45	25	71	19	97	14



Radiation from shear dislocation

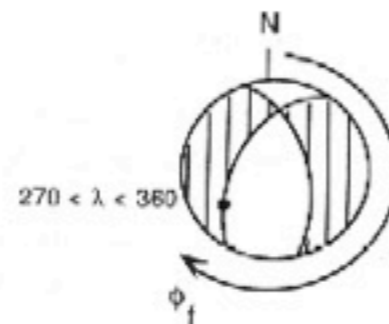
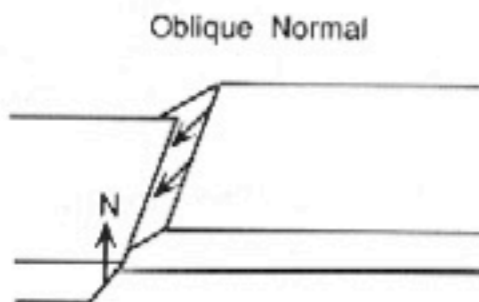
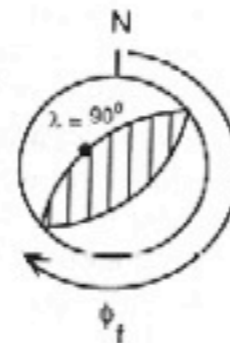
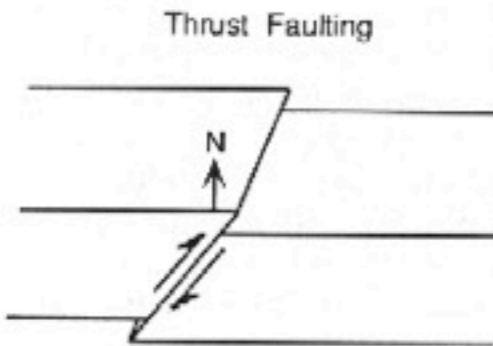
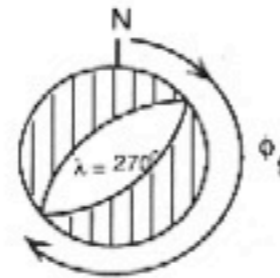
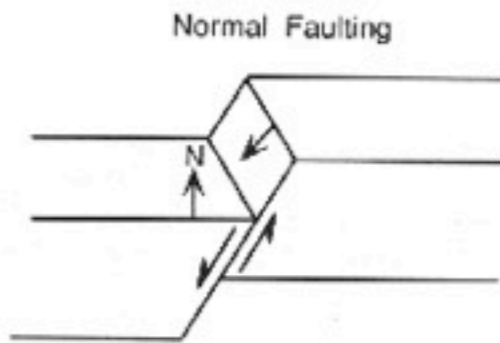
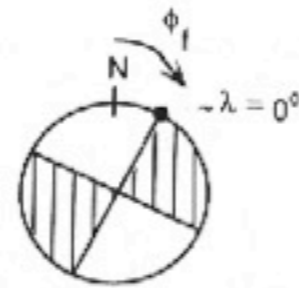
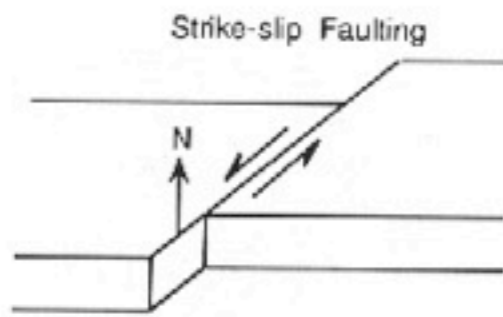


First motion of P waves at seismometers in various directions.

The polarities of the observed motion is used to determine the point source characteristics.

Beachballs always have two curved lines separating the quadrants, i.e. they show two planes. But there is only one fault plane and the other is called the auxiliary plane. Seismologists cannot tell which is which from seismograms alone, so we always show both of the possible solutions.

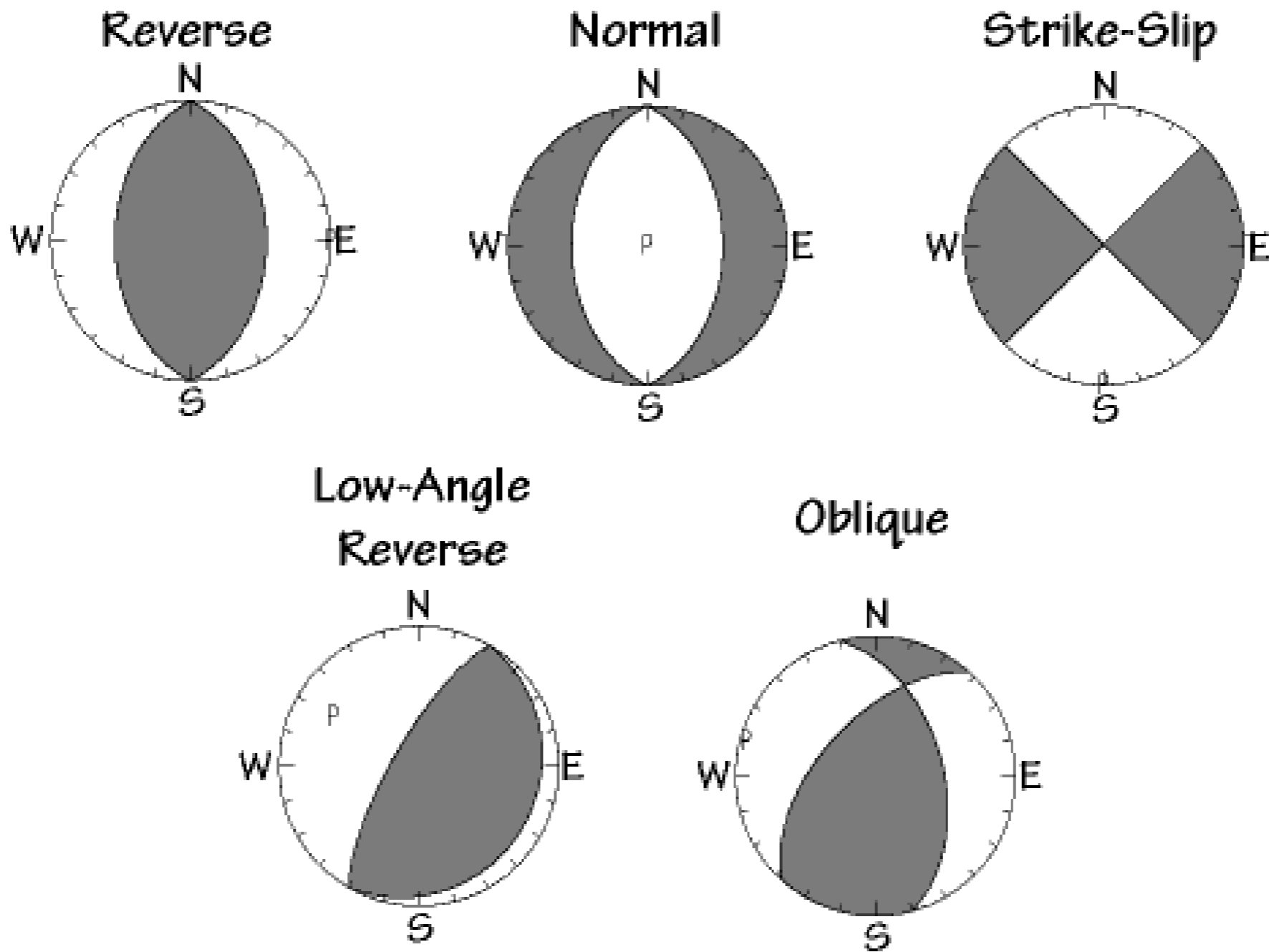
Fault types and focal mechanisms



Basis fault types and their appearance in the focal mechanisms. Dark regions indicate compressional P-wave motion.



The Principal Mechanisms

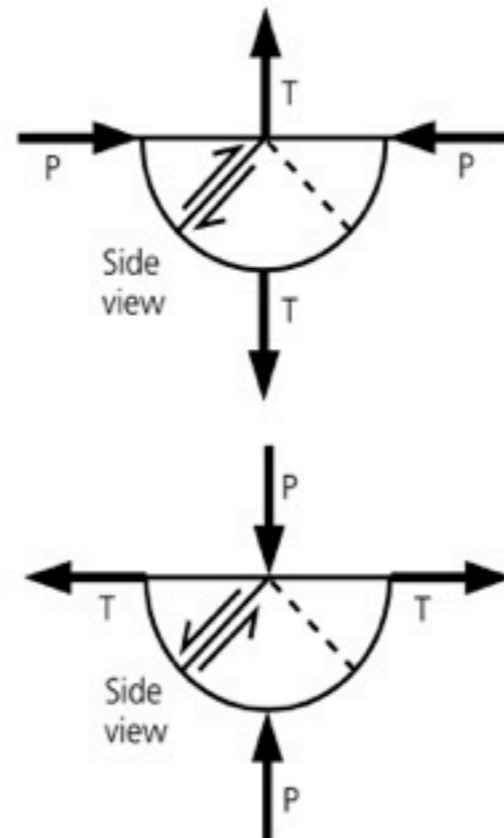
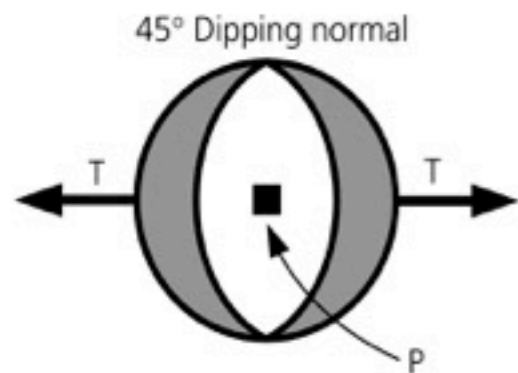
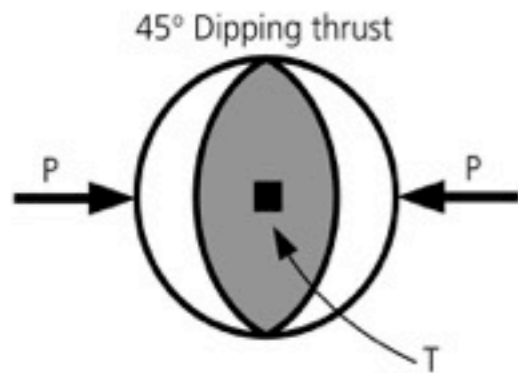
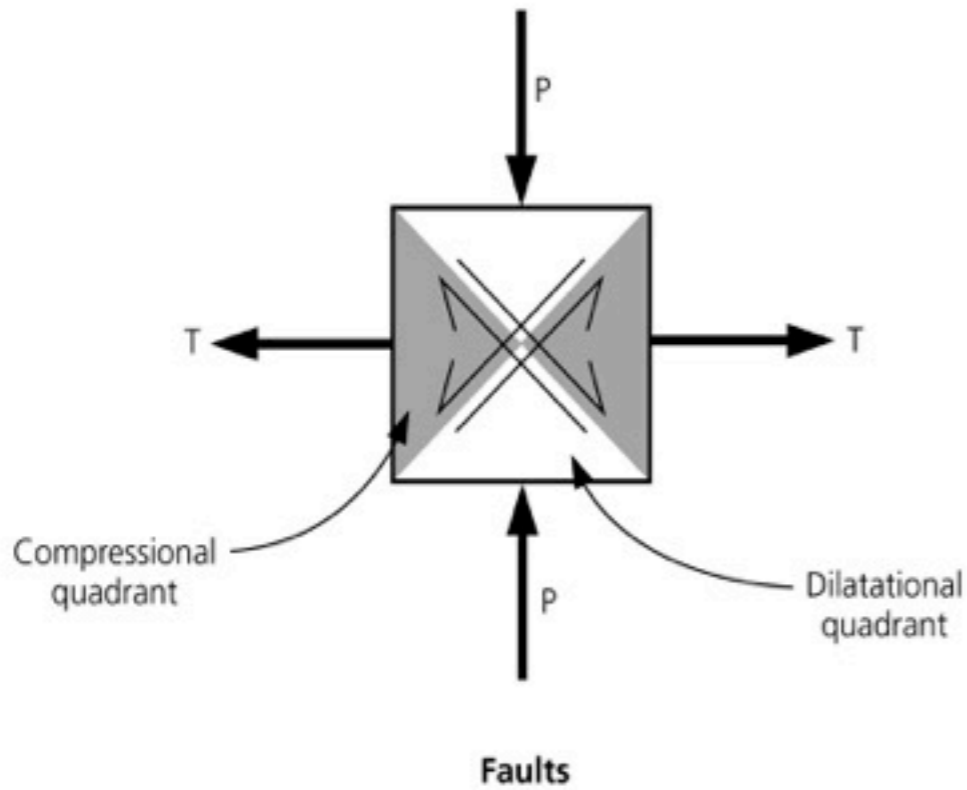




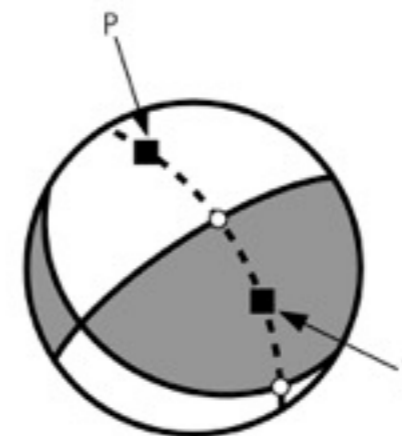
FM & stress axes



Figure 4.2-16: Relation between fault planes and stress axes.



To obtain P and T axes:



On the meridian connecting the poles, the points half-way between the nodal planes are the P and T axes

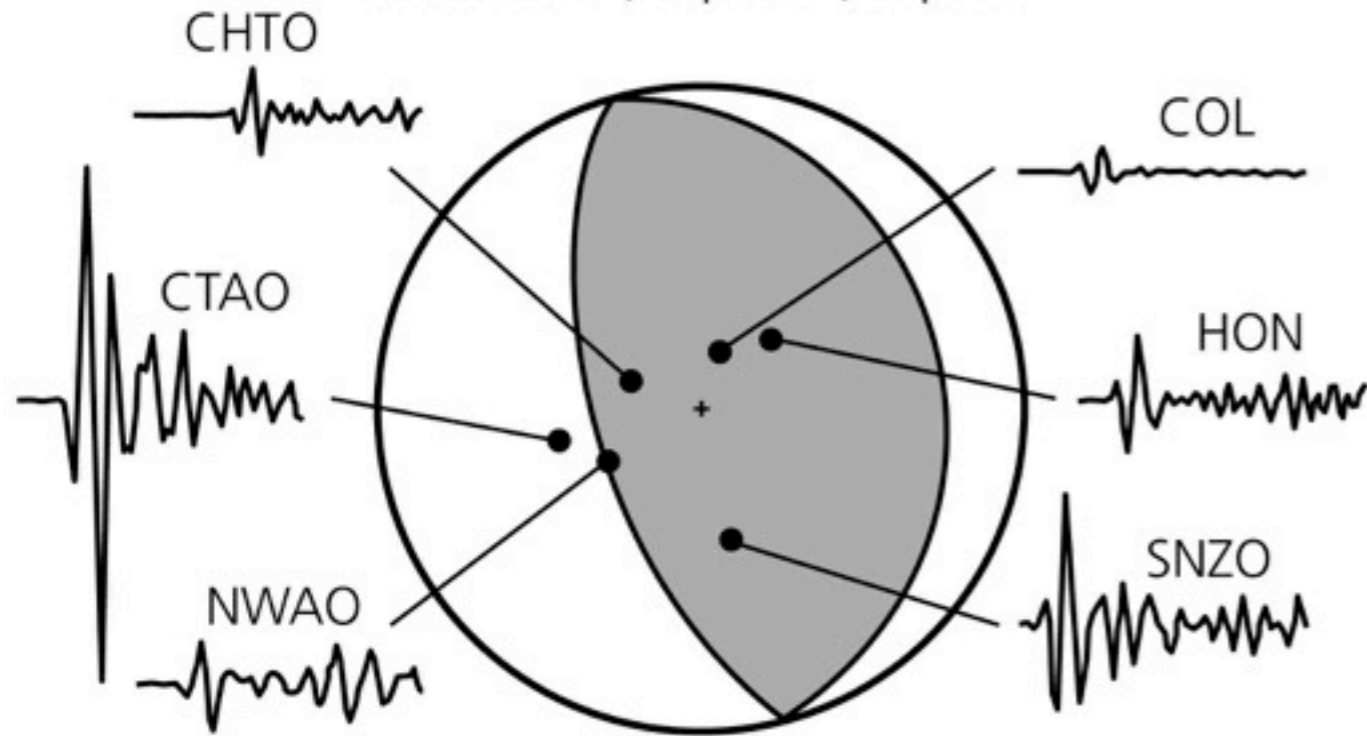


Figure 4.2-17: Examples of focal mechanisms and first motions.

Thrust faulting, Vanuatu Islands, July 3, 1985

Location: 17.2°S, 167.8°E. Depth: 30 km

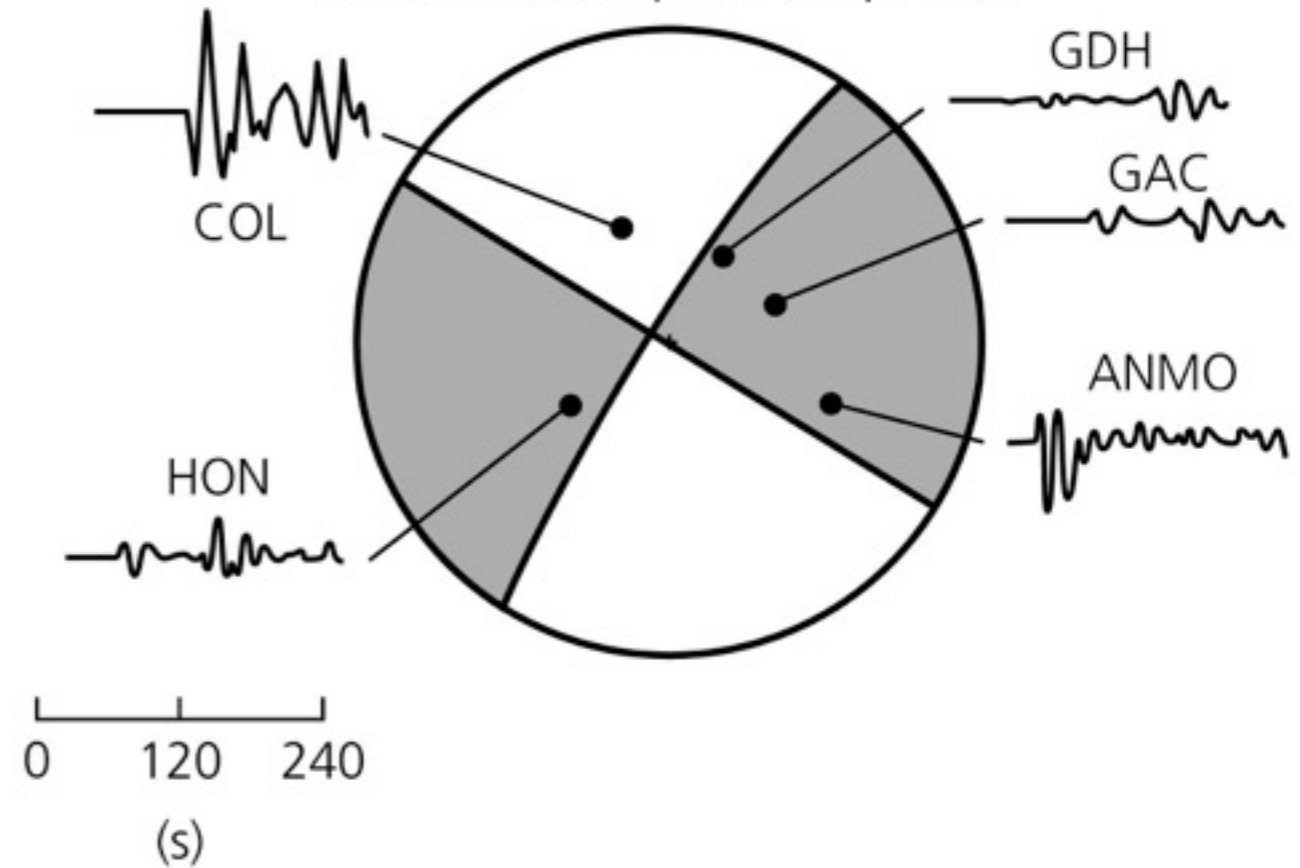
Strike: 352°, Dip: 26°, Slip: 97°



Strike-slip faulting, west of Oregon, March 13, 1985

Location: 43.5°N, 127.6°W. Depth: 10 km

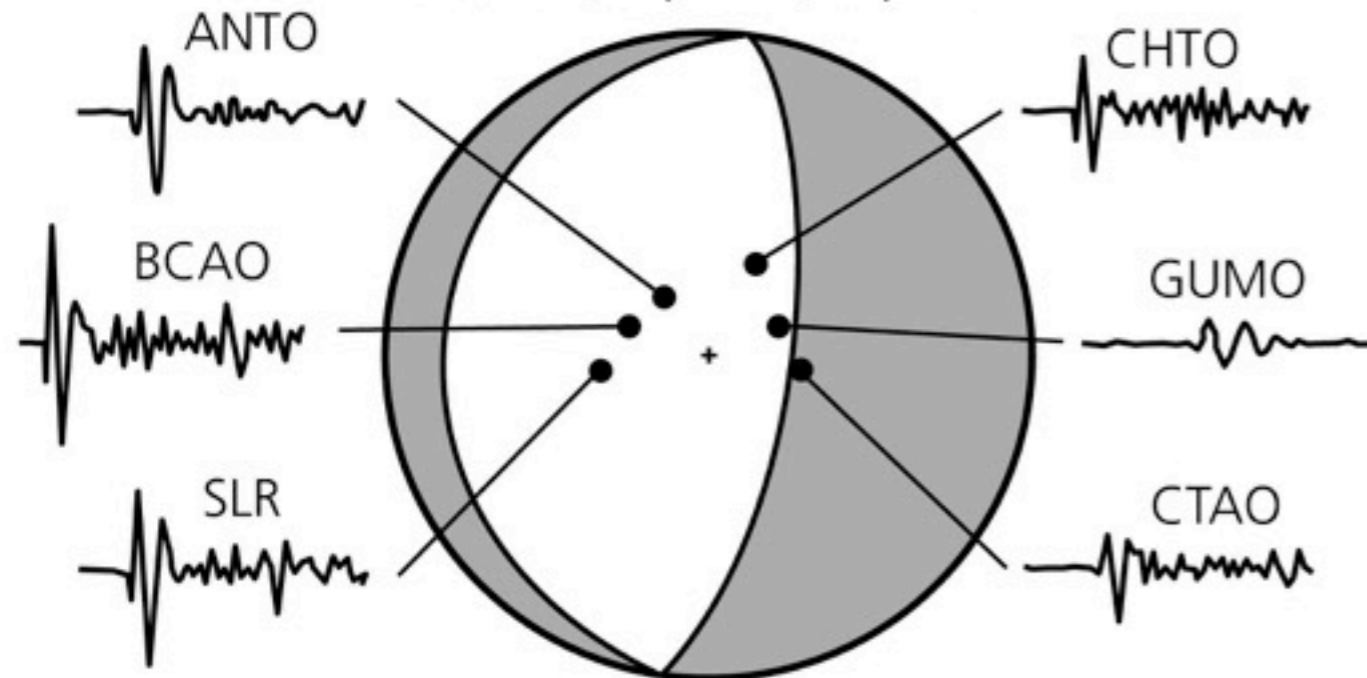
Strike: 302°, Dip: 90°, Slip: 186°



Normal faulting, mid-Indian rise, May 16, 1985

Location: 29.1°S, 77.7°E. Depth: 10 km

Strike: 8°, Dip: 70°, Slip: 270°



see also:

<http://www.learninggeoscience.net/free/00071/>



FM & Moment tensor



Figure 4.4-6: Selected moment tensors and their associated focal mechanisms.

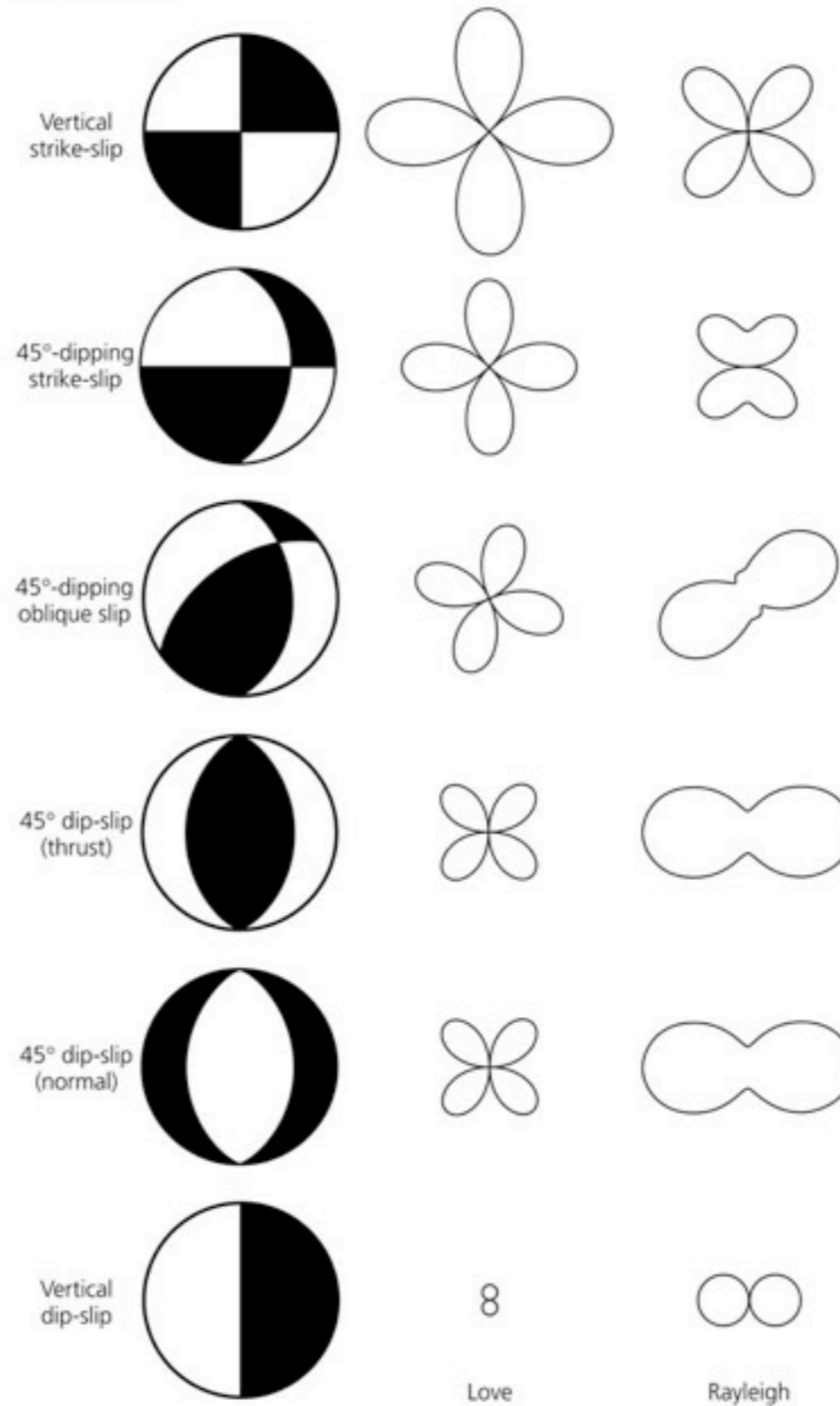
Moment tensor	Beachball	Moment tensor	Beachball
$\frac{1}{\sqrt{3}} \begin{pmatrix} 1 & 0 & 0 \\ 0 & 1 & 0 \\ 0 & 0 & 1 \end{pmatrix}$		$-\frac{1}{\sqrt{3}} \begin{pmatrix} 1 & 0 & 0 \\ 0 & 1 & 0 \\ 0 & 0 & 1 \end{pmatrix}$	
$-\frac{1}{\sqrt{2}} \begin{pmatrix} 0 & 1 & 0 \\ 1 & 0 & 0 \\ 0 & 0 & 0 \end{pmatrix}$		$\frac{1}{\sqrt{2}} \begin{pmatrix} 1 & 0 & 0 \\ 0 & -1 & 0 \\ 0 & 0 & 0 \end{pmatrix}$	
$\frac{1}{\sqrt{2}} \begin{pmatrix} 0 & 0 & -1 \\ 0 & 0 & 0 \\ -1 & 0 & 0 \end{pmatrix}$		$\frac{1}{\sqrt{2}} \begin{pmatrix} 0 & 0 & 0 \\ 0 & 0 & -1 \\ 0 & -1 & 0 \end{pmatrix}$	
$\frac{1}{\sqrt{2}} \begin{pmatrix} -1 & 0 & 0 \\ 0 & 0 & 0 \\ 0 & 0 & 1 \end{pmatrix}$		$\frac{1}{\sqrt{2}} \begin{pmatrix} 0 & 0 & 0 \\ 0 & -1 & 0 \\ 0 & 0 & 1 \end{pmatrix}$	
$\frac{1}{\sqrt{6}} \begin{pmatrix} 1 & 0 & 0 \\ 0 & -2 & 0 \\ 0 & 0 & 1 \end{pmatrix}$		$\frac{1}{\sqrt{6}} \begin{pmatrix} -2 & 0 & 0 \\ 0 & 1 & 0 \\ 0 & 0 & 1 \end{pmatrix}$	
$\frac{1}{\sqrt{6}} \begin{pmatrix} 1 & 0 & 0 \\ 0 & 1 & 0 \\ 0 & 0 & -2 \end{pmatrix}$		$-\frac{1}{\sqrt{6}} \begin{pmatrix} 1 & 0 & 0 \\ 0 & 1 & 0 \\ 0 & 0 & -2 \end{pmatrix}$	



Double couple RP & surface waves



Figure 4.3-12: Surface wave amplitude radiation patterns for several focal mechanisms.





Faults and Plates



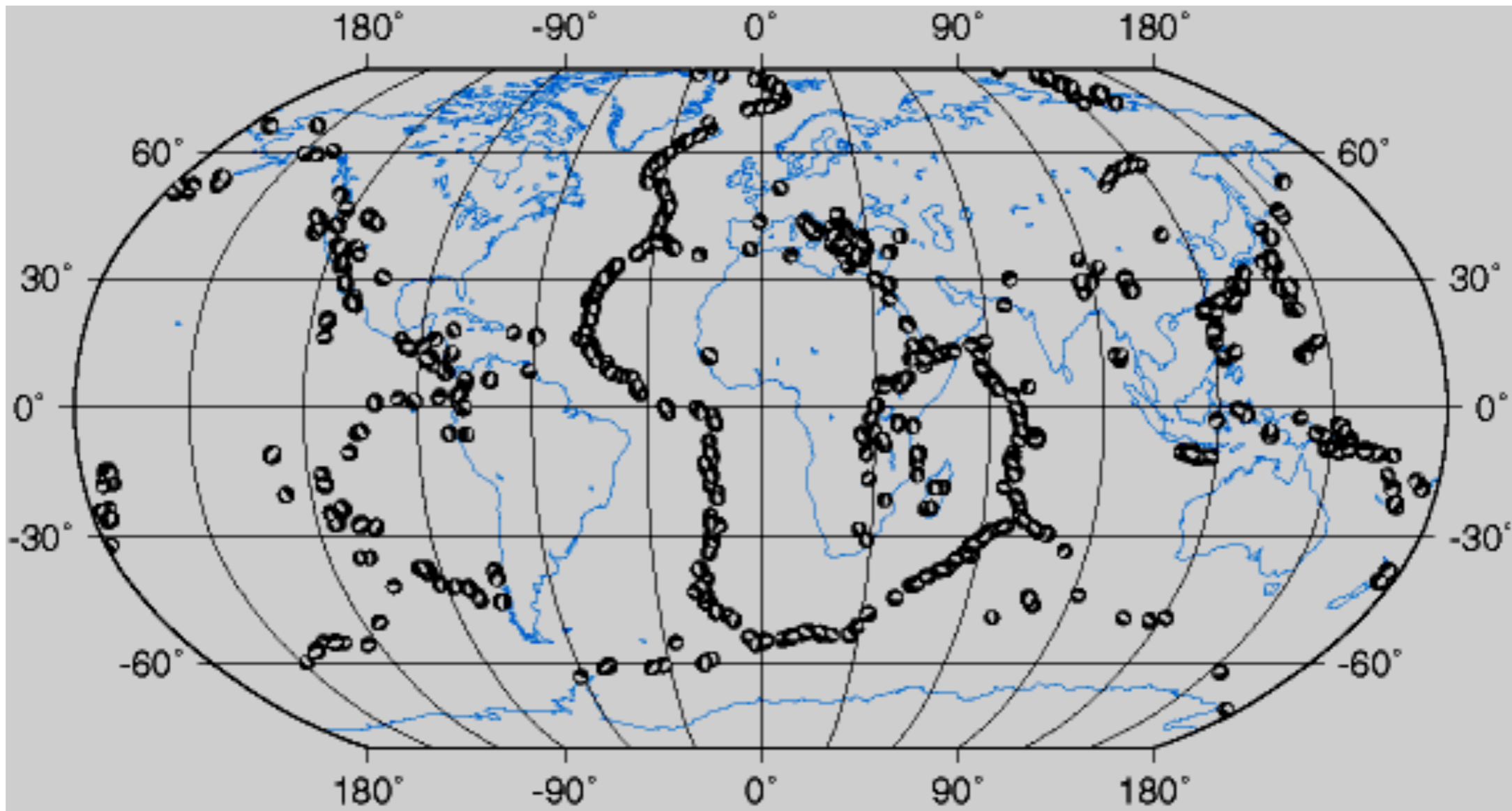
The style of faulting tells us something about the forces acting in a particular part of Earth.

Along plate boundaries, faulting reflects the motion of plates.

- Divergent Boundary = Normal Faulting
- Convergent Boundary = Reverse Faulting
- Transform Boundary = Strike-Slip Faulting

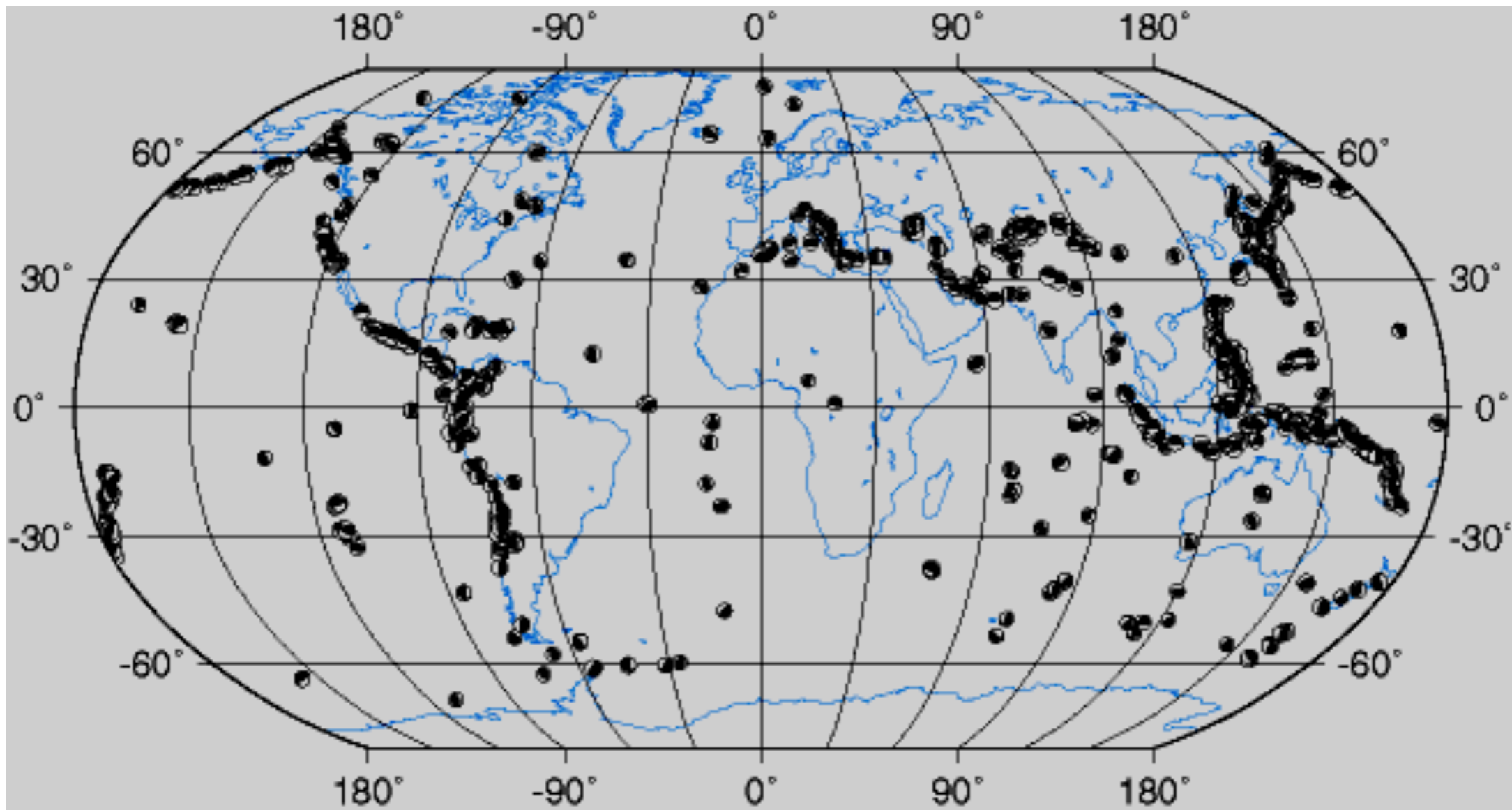


Where are the Normal Faults?



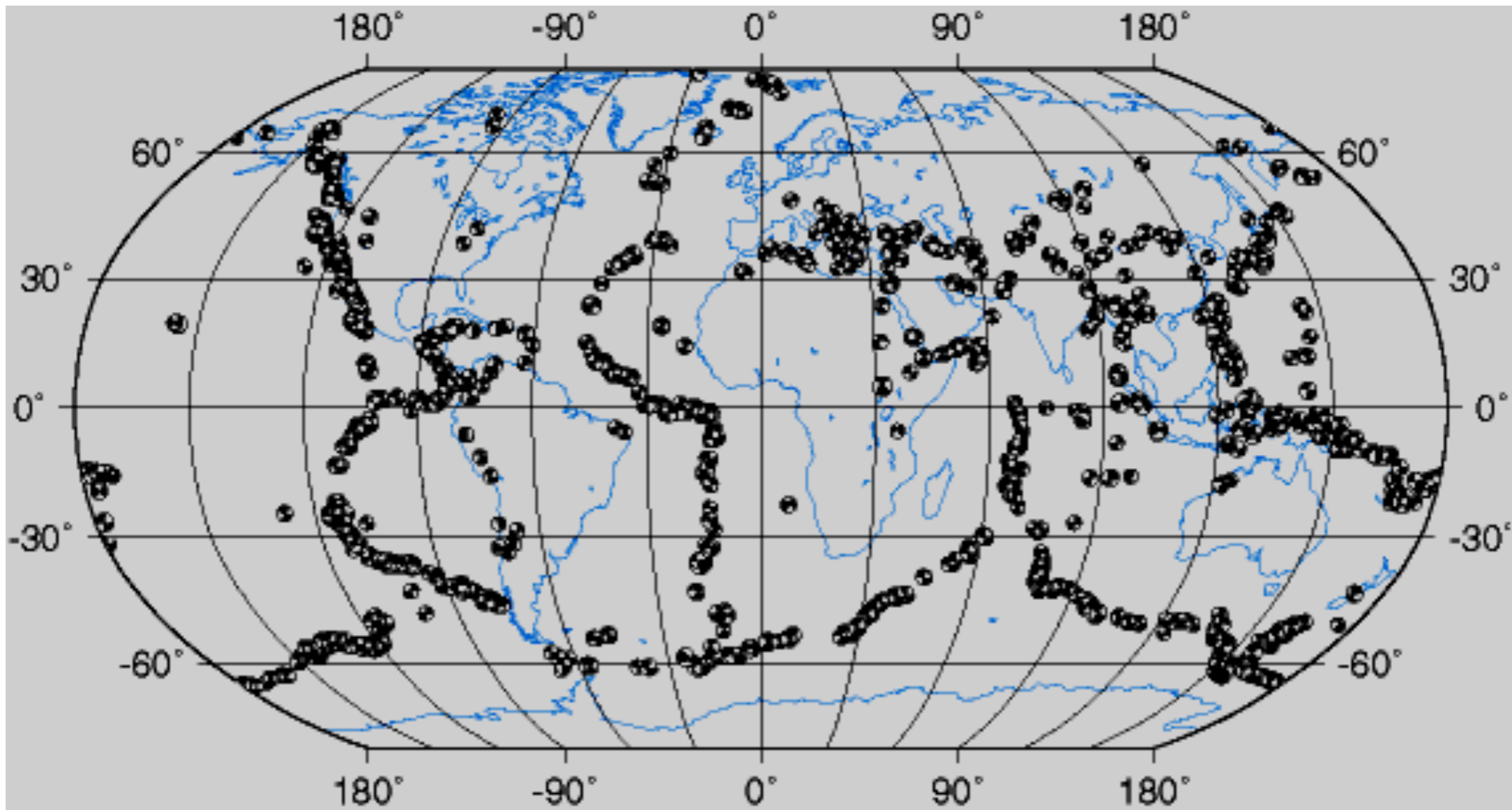


Where are the Reverse Faults?



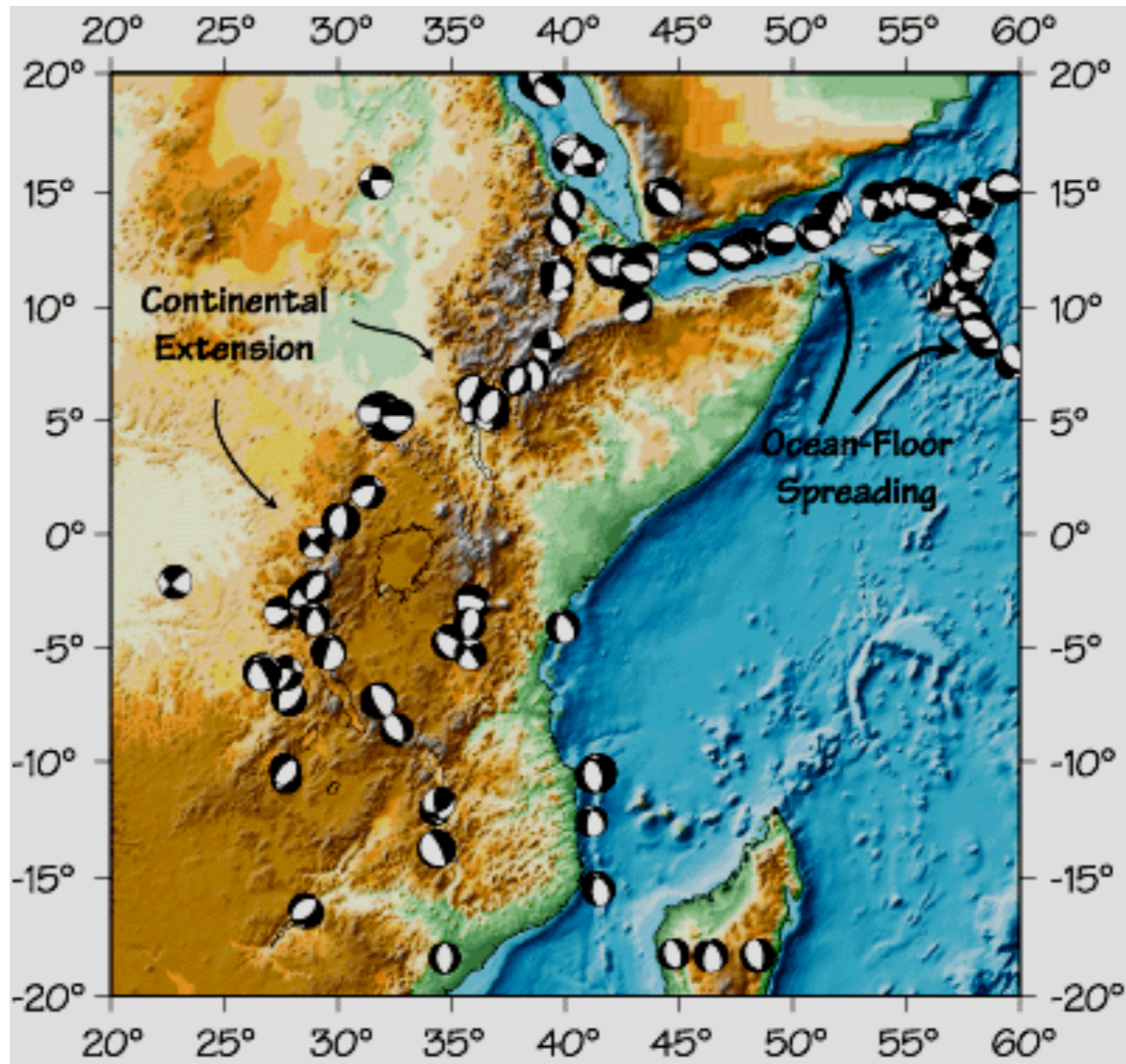


Where are the Transform Faults?





Example: East Africa





Faulting



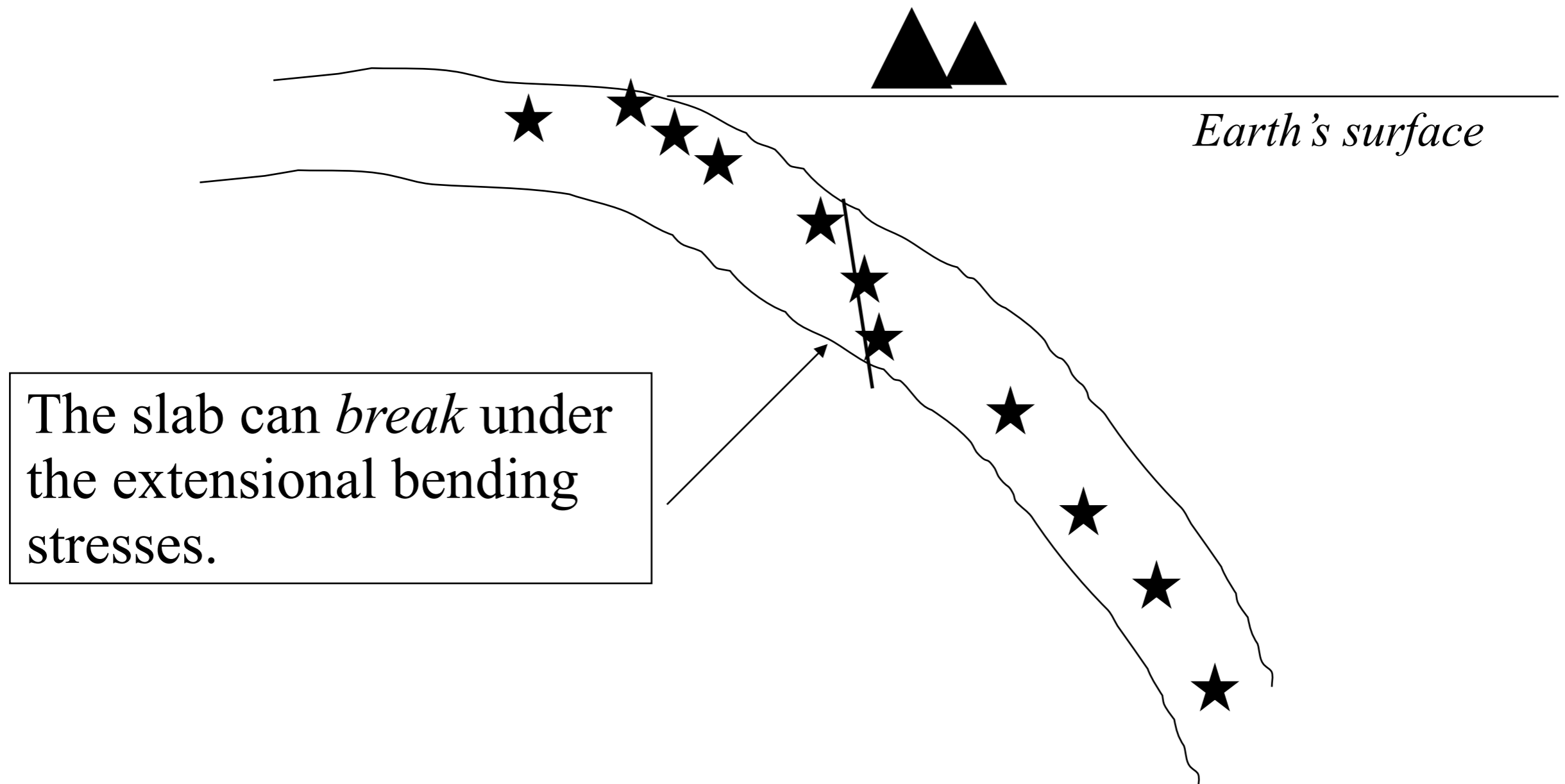
- So far we have talked about the faulting of shallow earthquakes, which are well explained by plate tectonics.
- What about the faulting style of deep earthquakes ?
- Do similar principles hold true?



Faulting



- We sometimes see "normal" faulting at depths of 100 km or so in subduction zones:

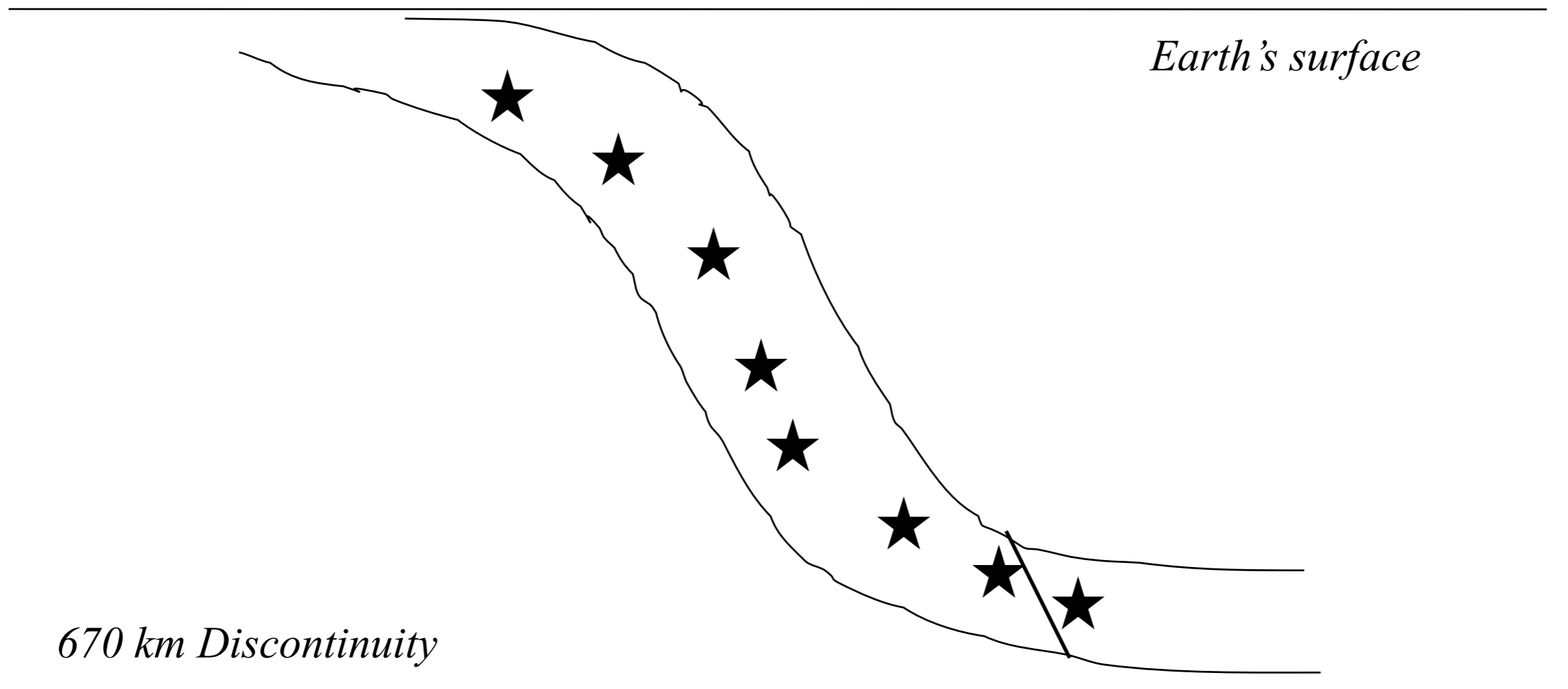




Faulting



- We sometimes see "reverse" faulting for the deepest earthquakes at about 600 km depth:



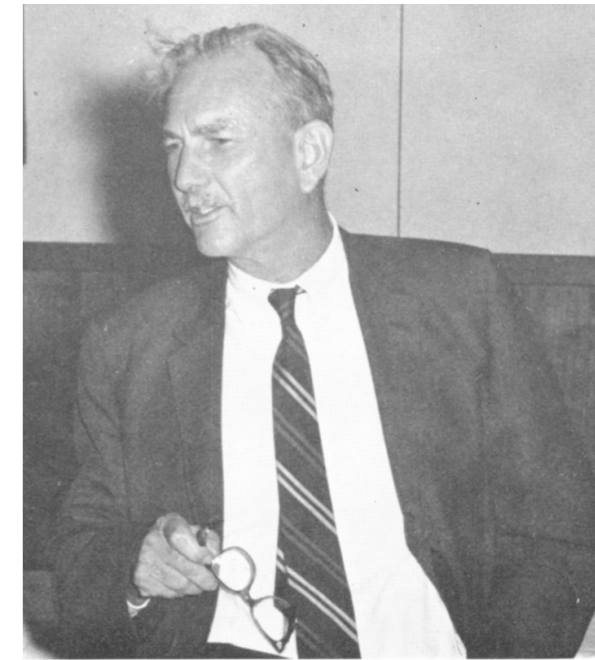
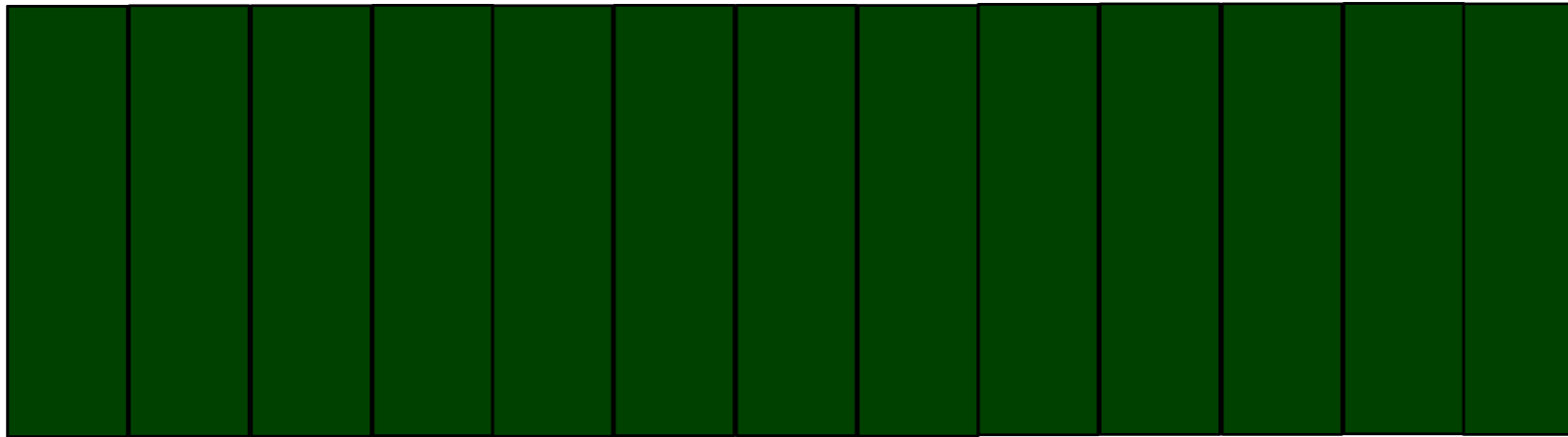


Haskell dislocation model



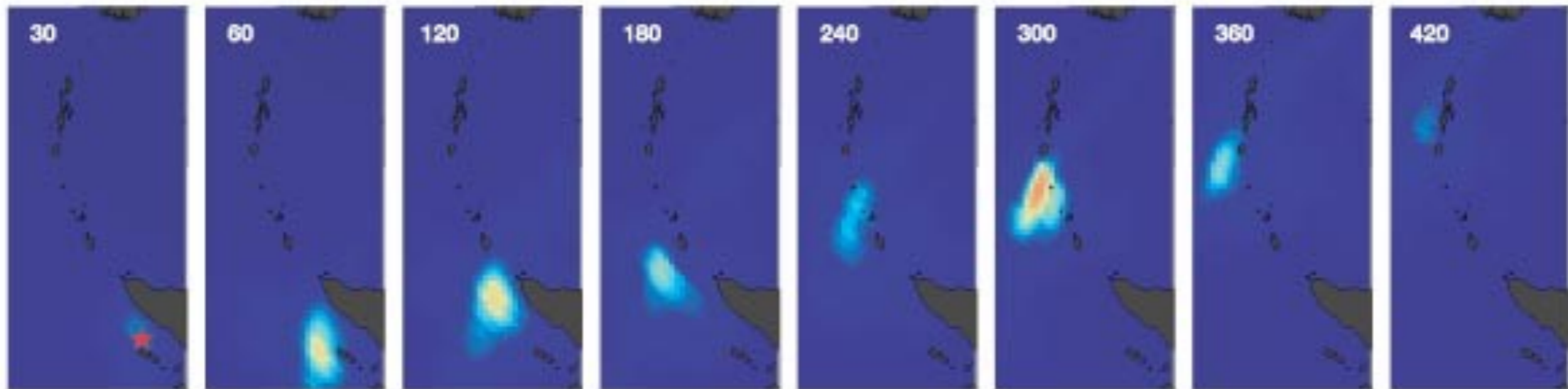
Haskell N. A. (1964). Total energy spectral density of elastic wave radiation from propagating faults, Bull. Seism. Soc. Am. **54**, 1811-1841

Rupture \longrightarrow



NORMAN A. HASKELL

Sumatra earthquake, Dec 28, 2004



Ishii et al., Nature 2005 doi:10.1038/nature03675



Haskell source model: far field

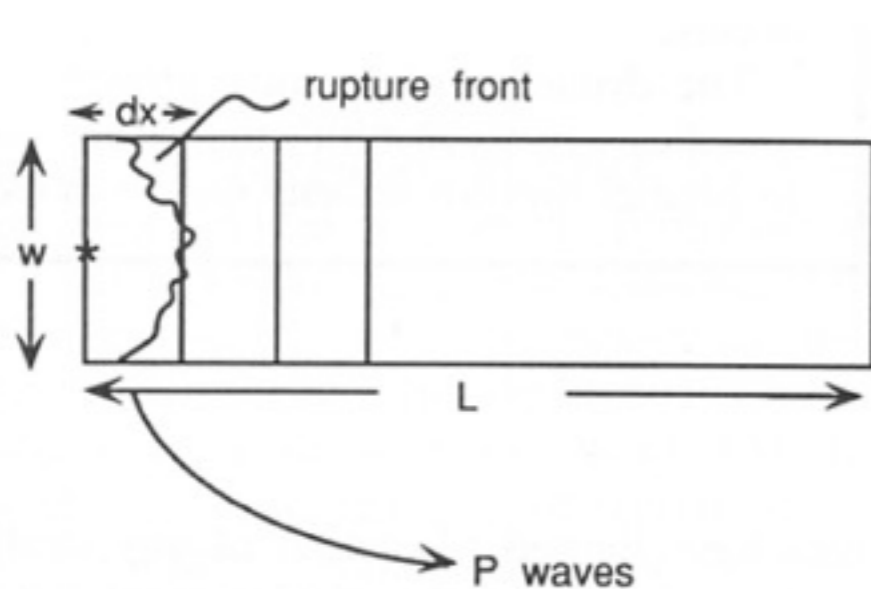


FIGURE 9.5 Geometry of a one-dimensional fault of width w and length L . The individual segments of the fault are of length dx , and the moment of a segment is $m dx$. The fault ruptures with velocity v_r .

$$u(x, t) = \frac{1}{4\pi\rho\alpha^3} (\sin 2\theta \cos \phi \hat{r}) \frac{\dot{M}(t - r/\alpha)}{r}$$

$$\begin{aligned} u_r(r, t) &= \sum_{i=1}^N u_i(r_i, t - r_i/\alpha - \Delta t_i) = \\ &= \frac{R_i^P \mu}{4\pi\rho\alpha^3} W \sum_{i=1}^N \frac{\dot{D}_i}{r_i} (t - \Delta t_i) dx \approx \\ &\approx \frac{R_i^P \mu}{4\pi\rho\alpha^3} \frac{W}{r} \sum_{i=1}^N \dot{D}(t) * \delta\left(t - \frac{x}{v_r}\right) dx \approx \\ &\approx \frac{R_i^P \mu}{4\pi\rho\alpha^3} \frac{W}{r} \dot{D}(t) * \int_0^L \delta\left(t - \frac{x}{v_r}\right) dx = \\ &= \frac{R_i^P \mu}{4\pi\rho\alpha^3} \frac{W}{r} v_r \dot{D}(t) * B(t; T_r) \end{aligned}$$



Haskell source model: far field



$$u_r(r,t) \propto \dot{D}(t) * v_r H(z) \Big|_{t-x/v_r}^t = v_r \dot{D}(t) * B(t; T_r)$$

resulting in the convolution of two boxcars: the first with duration equal to the rise time and the second with duration equal to the rupture time (L/v_r)

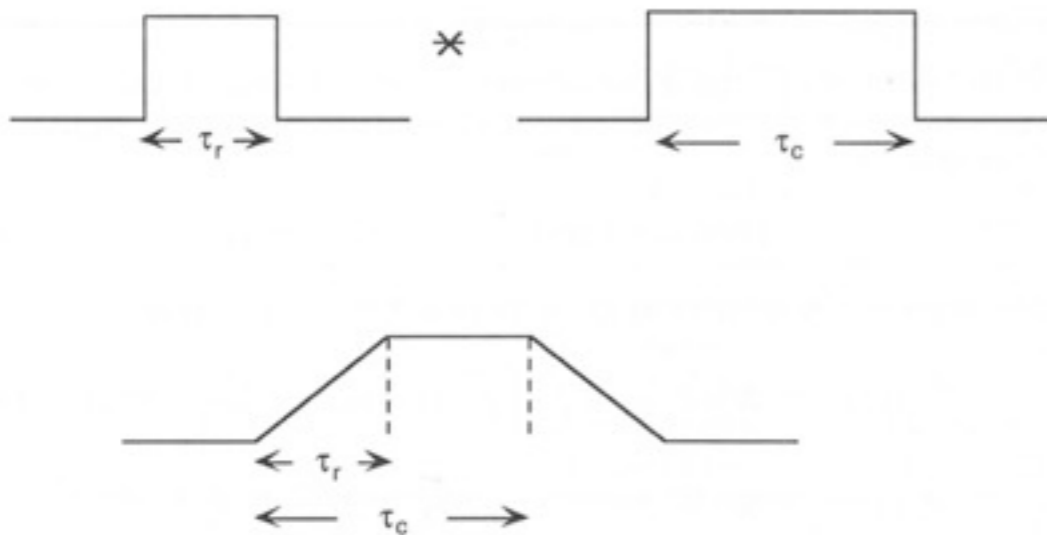


FIGURE 9.6 The convolution of two boxcars, one of length τ_r and the other of length τ_c ($\tau_c > \tau_r$). The result is a trapezoid with a rise time of τ_r , a top of length $\tau_c - \tau_r$, and a fall of width τ_r .

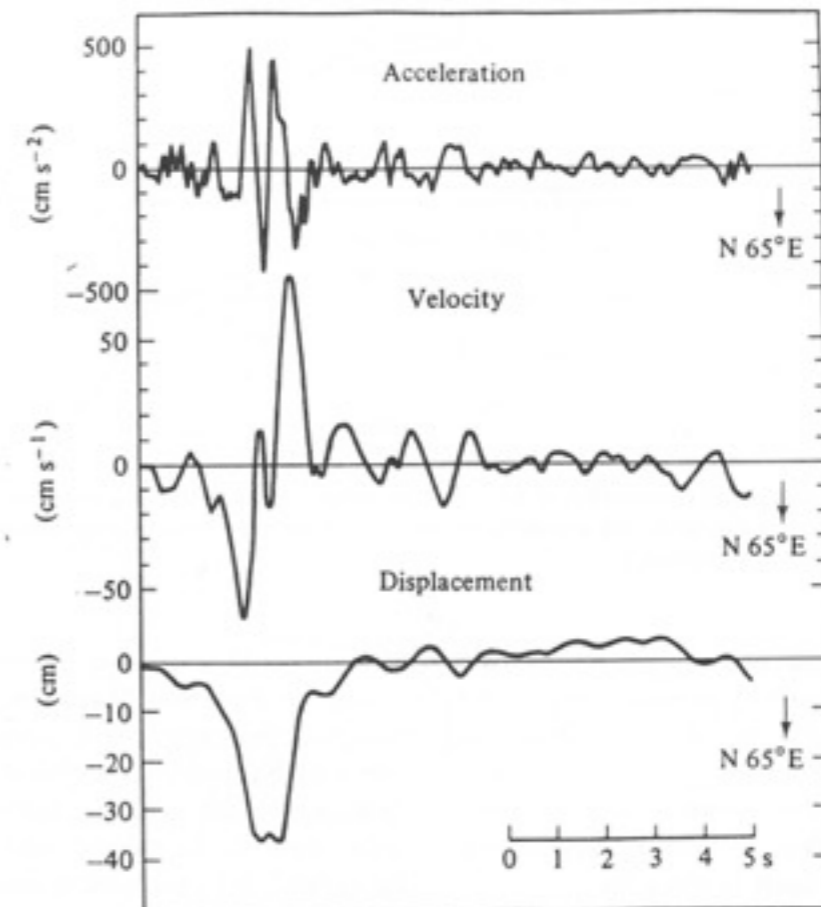
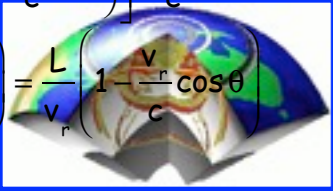


FIGURE 9.7 A recording of the ground motion near the epicenter of an earthquake at Parkfield, California. The station is located on a node for P waves and a maximum for SH . The displacement pulse is the SH wave. Note the trapezoidal shape. (From Aki, *J. Geophys. Res.* 73, 5359-5375, 1968; © copyright by the American Geophysical Union.)

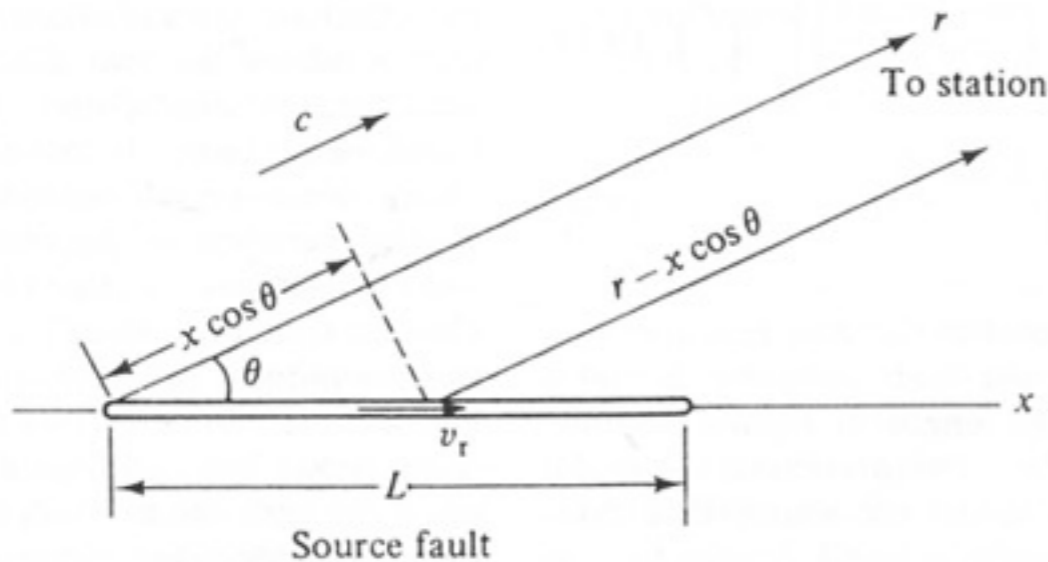


Haskell source model: directivity



The body waves generated from a breaking segment will arrive at a receiver before than those that are radiated by a segment that ruptures later.

If the path to the station is not perpendicular, the waves generated by different segments will have different path lengths, and then unequal travel times.



$$T_r = \left[\frac{L}{v_r} + \left(\frac{r - L \cos \theta}{c} \right) \right] - \frac{r}{c} =$$

$$= \frac{L}{v_r} - \left(\frac{L \cos \theta}{c} \right) = \frac{L}{v_r} \left(1 - \frac{v_r}{c} \cos \theta \right)$$

FIGURE 9.8 Geometry of a rupturing fault and the path to a remote recording station. (From Kasahara, 1981.)

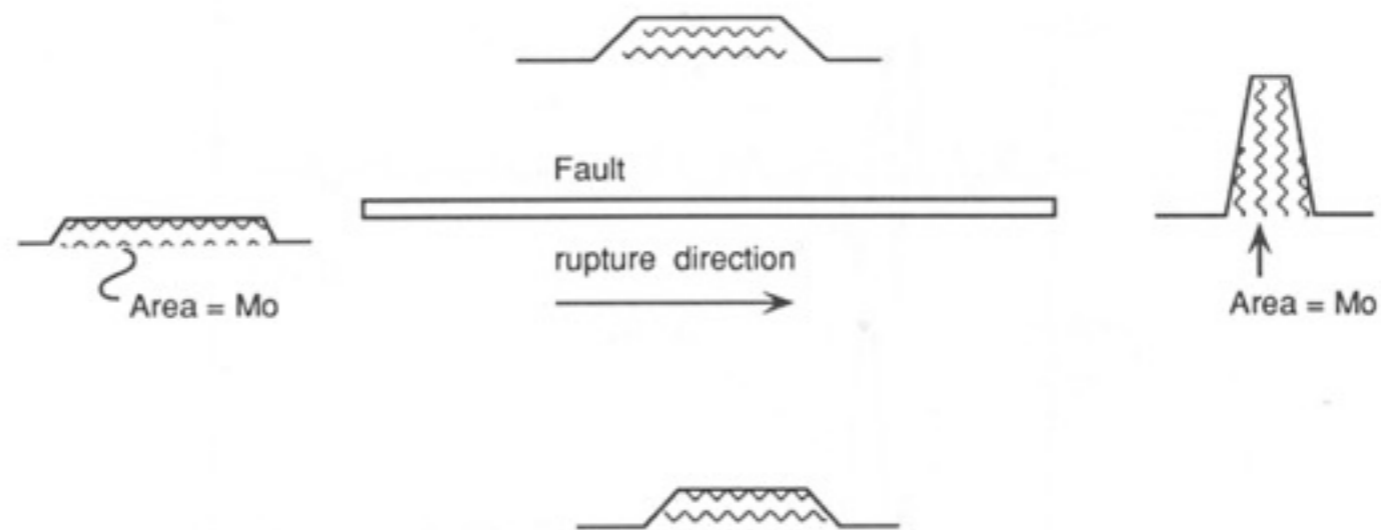


FIGURE 9.9 Azimuthal variability of the source time function for a unilaterally rupturing fault. The duration changes, but the area of the source time function is the seismic moment and is independent of azimuth.



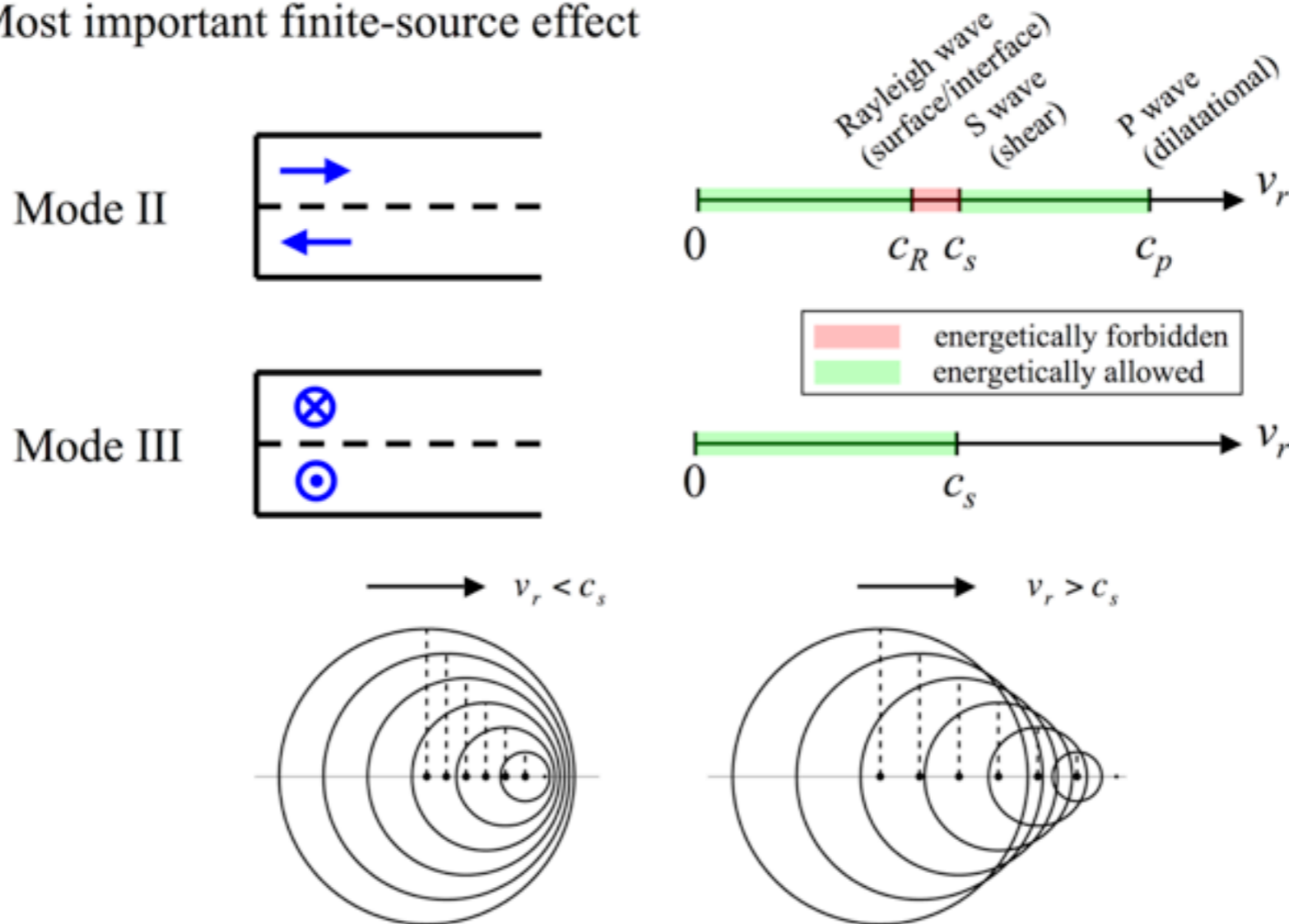
Rupture velocity



Earthquake ruptures typically propagate at velocities that are in the range 70-90% of the S-wave velocity and this is independent of earthquake size. A small subset of earthquake ruptures appear to have propagated at speeds greater than the S-wave velocity. These **supershear earthquakes** have all been observed during large strike-slip events.

Rupture Velocity and Directivity:

Most important finite-source effect



<http://pangea.stanford.edu/~edunham/research/supershear.html>



Directivity example

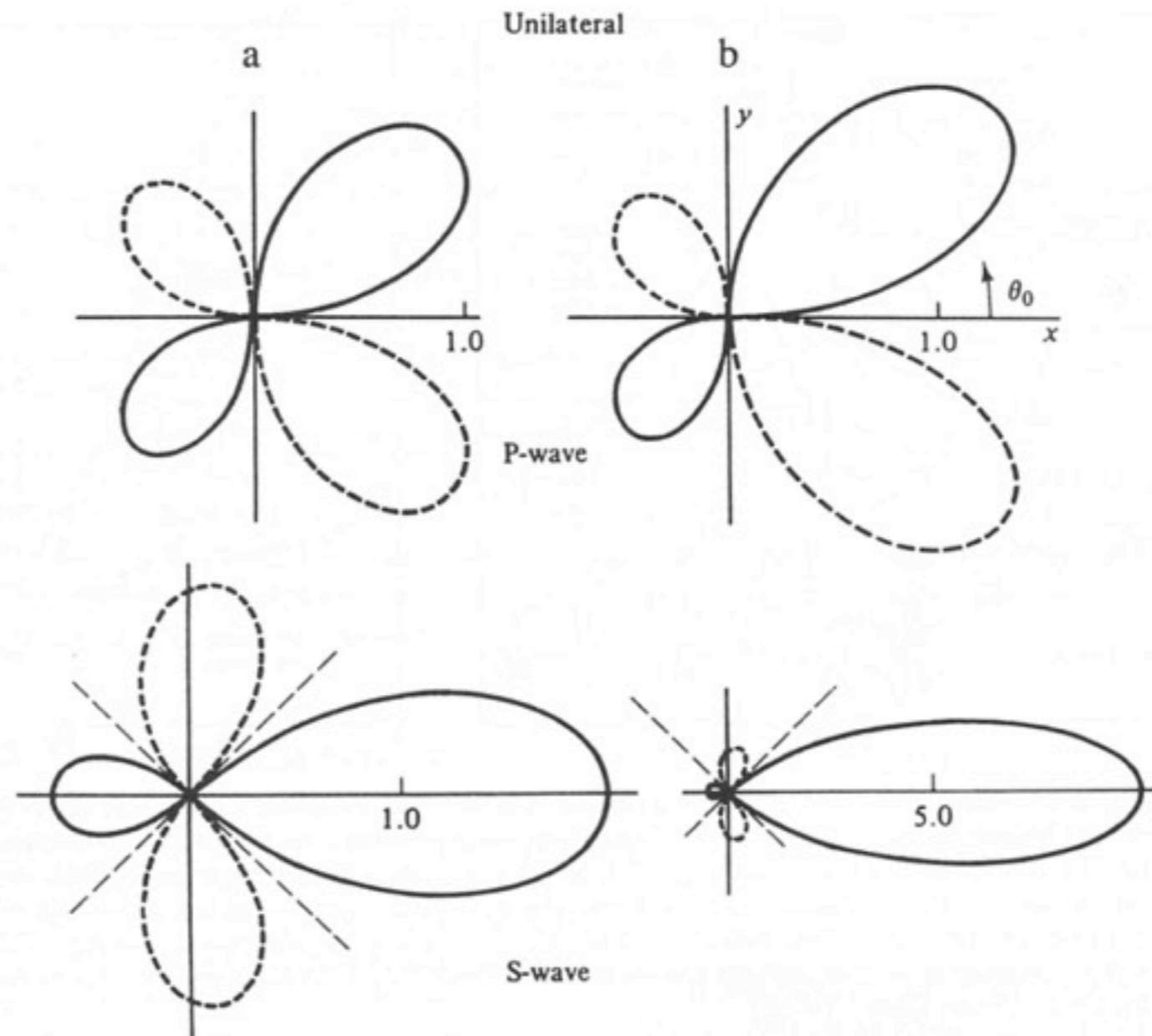


FIGURE 9.10 The variability of *P*- and *SH*-wave amplitude for a propagating fault (from left to right). For the column on the left $v_r/v_s = 0.5$, while for the column on the right $v_r/v_s = 0.9$. Note that the effects are amplified as rupture velocity approaches the propagation velocity. (From Kasahara, 1981.)



Ground motion scenarios



Surface Cumulative Peak Velocity Magnitude (3 sec)

■ PeakVelocity:0.0005 Lat:-117.4650 Long:34.2758

■ PeakVelocity:0.0004 Lat:-115.6840 Long:33.3579



Simulation2 (NW-SE)



Simulation3 (SE-NW)

100 km

The two views in this movie show the cumulative velocities for a San Andreas earthquake TeraShake simulation, rupturing south to north and north to south. The crosshairs pinpoint the peak velocity magnitude as the simulation progresses.

www.scec.org



Source spectrum



The displacement pulse, corrected for the geometrical spreading and the radiation pattern can be written as:

$$u(t) = M_0 \left(B(t; \tau) * B(t; T_R) \right)$$

and in the frequency domain:

$$U(\omega) = M_0 F(\omega) = M_0 \left| \frac{\sin\left(\frac{\omega\tau}{2}\right)}{\left(\frac{\omega\tau}{2}\right)} \right| \left| \frac{\sin\left(\frac{\omega L}{v_r 2}\right)}{\left(\frac{\omega L}{v_r 2}\right)} \right| \approx \begin{cases} M_0 & \omega < \frac{2}{T_r} \\ \frac{2M_0}{\omega T_R} & \frac{2}{T_r} < \omega < \frac{2}{\tau} \\ \frac{4M_0}{\omega^2 \tau T_R} & \omega > \frac{2}{\tau} \end{cases}$$



Source spectrum



Figure 4.6-4: Approximation of the $(\sin x)/x$ function, and derivation of corner frequencies.

